# **GEOSPHERE**

**GEOSPHERE** 

https://doi.org/10.1130/GES02400.1

13 figures; 5 tables; 1 set of supplemental files

CORRESPONDENCE: ioshua.schwartz@csun.edu

CITATION: Brackman, A.J., and Schwartz, J.J., 2022, The formation of high-Sr/Y plutons in cordilleran-arc crust by crystal accumulation and melt loss: Geohttps://doi.org/10.1130 /GES02400.1.

Science Editor: Shanaka de Silva Associate Editor: Alan Whittington

Received 14 January 2021 Revision received 5 July 2021 Accepted 4 October 2021

Published online 11 February 2022





This paper is published under the terms of the CC-BY-NC license

© 2022 The Authors

# The formation of high-Sr/Y plutons in cordilleran-arc crust by crystal accumulation and melt loss

Adam J. Brackman and Joshua J. Schwartz

Department of Geological Sciences, California State University Northridge, Northridge, California 91330, USA

# **ABSTRACT**

Bulk-rock data are commonly used in geochemical studies as a proxy for melt compositions in order to understand the evolution of crustal melts. However, processes of crystal accumulation and melt migration out of deep-crustal, crystal-rich mush zones to shallower storage regions raise questions about how faithfully bulk-rock compositions in plutons approximate melt compositions. This problem is particularly acute in the lower crust of arcs, where melt reservoirs are subject to periodic melt extraction that leaves behind a cumulate residue. Here, we examine bulk-rock data from the perspective of high-Sr/Y plutonic rocks in the lower crust of a well-exposed Early Cretaceous cordilleran-arc system in Fiordland, New Zealand. We test the validity of using high-Sr/Y bulk-rock compositions as proxies for melts by comparing bulk-rock compositions to melts modeled from >100 major- and trace-element analyses of 23 magmatic clinopyroxene grains from the same samples. The sampling locations of the igneous clinopyroxenes and encompassing bulk rocks are distributed across ~550 km2 of exhumed lower crust and are representative of Mesozoic lower-crustal arc rocks in the Median batholith.

We confirm that bulk-rock data have characteristics of high-Sr/Y plutons (Sr/Y >50, Na<sub>2</sub>O >3.5 wt%, Sr >1000 ppm, and Y <20 ppm), features that have been previously interpreted to indicate the presence of garnet as a residual or fractionating phase. In contrast to bulk rocks, igneous clinopyroxenes have low Sr (<100 ppm), high Y (25–100 ppm), and low molar Mg# [100 x Mg/(Mg + Fe)] values (60-70), which are consistent with derivation from fractionated, low-Sr/Y melts. Chondrite-normalized rare-earth-element patterns and Sm/Yb values in clinopyroxenes also show little to no evidence for involvement of garnet in the source or in differentiation processes. Fe-Mg partitioning relationships indicate that clinopyroxenes are not in equilibrium with their encompassing bulk rocks but could have been in equilibrium with melt compositions determined from chemometry of coexisting igneous hornblendes. Moho-depth calculations based on bulk-rock Sr/Y values also yield Moho depths (average = 69 km) that are inconsistent with Moho depths based on bulk-rock Ce/Y, contact aureole studies, Al-in-hornblende crystallization pressures, and our modeled clinopyroxene crystallization pressures. These data indicate that most Mesozoic high-Sr/Y bulk rocks in the lower crust of Fiordland are cumulates formed by plagioclase + amphibole + clinopyroxene accumulation and interstitial melt loss from crystal-rich mush

zones. Our data do not support widespread fractionation of igneous garnet nor partial melting of a garnet-bearing source in the petrogenesis of these melts. We speculate that melt extraction and the production of voluminous cumulates in the lower crust were aided by unusually high heat flow and high magma addition rates associated with an Early Cretaceous arc flareup. We conclude that bulkrock compositions are poor proxies for melt compositions in the lower crust of the Median batholith, and geochemical modeling of these high-Sr/Y bulk rocks would overemphasize the role of garnet in their petrogenesis.

# INTRODUCTION

Subduction zones are commonly considered to be factories for the generation of continental crust, and cordilleran batholiths are the products of subductionrelated magmatism in the roots of continental arcs (Taylor and McLennan, 1995, 1985; Rudnick, 1995; Kelemen, 1995; Hawkesworth and Kemp, 2006; Kelemen et al., 2014). In geochemical studies of cordilleran batholiths, bulk-rock geochemistry is commonly used as a means of reconstructing melts that were involved in crust creation. A key problem with this approach is that plutonic rocks form in complex mush zones that are subject to a variety of processes involving in situ crystal fractionation, injection and/or replenishment from externally derived magmas, assimilation of wall rock, and melt migration to shallower storage regions. The fact that these processes occur in evolving magma mushes in the roots of arcs raises questions about how faithfully bulk-rock compositions in cordilleran plutons and batholiths realistically approximate melt compositions.

The use of bulk-rock geochemical data in understanding cordilleran-arc processes is highlighted in recent studies that use Sr/Y values as a proxy for paleo-crustal thickness (Chiaradia, 2015; Chapman et al., 2015; Profeta et al., 2015). The Sr/Y proxy is based on the contrasting behavior of Sr and Y during crustal melting and relies on their pressure-sensitive behavior. For example, at low pressures (<1.0 GPa), Sr strongly partitions into plagioclase, whereas at high pressures (>1.2 GPa), Sr preferentially enters the melt because plagioclase is unstable at deep crustal pressures. Conversely, at low pressures, Y prefers to enter the melt phase, and at high pressures, it preferentially enters either garnet or amphibole. The result is that Sr/Y is commonly considered to be a pressure-sensitive indicator of the depth of melting in cordilleran arc crust and it has thus been used as a tool for understanding the evolution of orogenic belts through time (Tulloch and Kimbrough, 2003; Karlstrom et al., 2014; Chapman et al., 2015; Profeta et al., 2015;

Joshua Schwartz https://orcid.org/0000-0002-8385-2705

Kirsch et al., 2016; Ardill et al., 2018). This concept relies on two basic assumptions that we evaluate here: (1) Sr/Y values in bulk rocks are reliable indicators of original melt compositions, and (2) high-Sr/Y melts form from intracrustal partial melting in the presence of garnet. In addition to intracrustal partial melting, a wide variety of other mechanisms are also possible for producing high-Sr/Y signatures, including melting of a young subducting oceanic crust (Defant and Drummond, 1990), fractionation of garnet at high pressure in the lower crust or upper mantle (Petford and Atherton, 1996), and/or melt extraction leaving behind a plagioclase-rich cumulate (Turnbull et al., 2010; Laurent, et al., 2020). These various models are illustrated schematically in Figures 1A–1D.

Besides using bulk-rock values themselves, another approach to understanding the significance of Sr/Y values is to directly examine the composition of igneous minerals in bulk rocks and model predicted melt compositions from appropriate partition coefficients (Luhr and Carmichael, 1980; Sisson, 1991; Ewart and Griffin; 1994; Blundy et al., 1998; Green et al., 2000; Wood and Trigila, 2001; Severs et al., 2009). In a study of Aleutian adakites (Alaska, USA), Yogodzinski and Kelemen (1998) demonstrated that clinopyroxenes also recorded high-Sr/Y signatures as observed in bulk-rock lava compositions. To date, there have been few similar studies of cordilleran arc crust, which raises the guestion of whether high-Sr/Y bulk-rock values in circum-Pacific batholiths faithfully preserve information about melt compositions or whether their values reflect other processes (including melt loss and/or crystal accumulation). The significance of high-Sr/Y plutonic rocks in cordilleran arcs has implications for changes in crustal thickness through time, the production (or not) of dense, garnet-bearing arc roots (e.g., arclogite; Fig. 1C; Ducea et al., 2020a, 2020b), and the ways in which continental crust is created in the deep crust of arcs.

Here, we examine high-Sr/Y plutonic rocks in the Median batholith, a long-lived cordilleran arc in New Zealand (e.g., Muir et al., 1995; Mortimer et al., 1999; Tulloch and Kimbrough, 2003; Milan et al., 2017; Schwartz et al., 2017, 2021). These rocks formed along the paleo-Pacific margin of Gondwana in the Early Cretaceous and represent the inboard component of a paired high- and low-Sr/Y cordilleran arc (Tulloch and Kimbrough, 2003). The high-Sr/Y arc rocks are exhumed as >3000 km² of arc crust in the Fiordland segment of the Median batholith and are particularly abundant in the lower-crustal Western Fiordland Orthogneiss where they make up >50% of the crust (see orange and red plutons in Fig. 2A) (Milan et al., 2017; Schwartz et al., 2017; Klepeis et al., 2019). Relict igneous assemblages including clinopyroxene are common in many of these rocks (e.g., Klepeis et al., 2016), and their preservation presents an opportunity for examining the significance of high-Sr/Y signatures in cordilleran arc crust from the igneous mineral perspective.

# ■ GEOLOGIC BACKGROUND

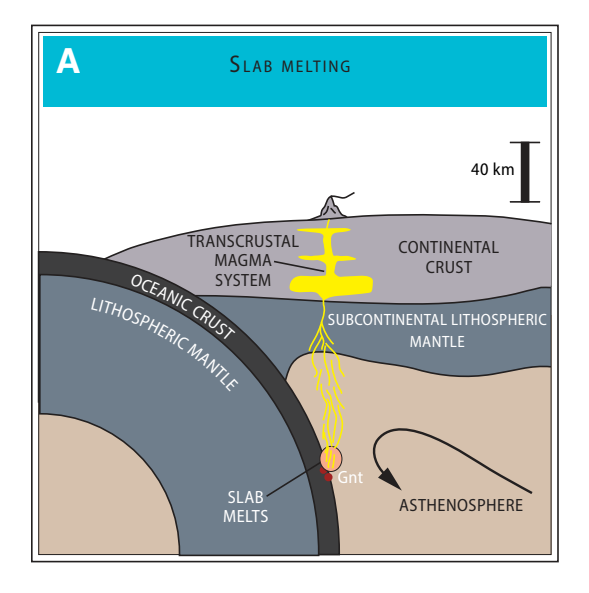
Zealandia–Te Riu-a-Māui, Earth's most-recently recognized continent, was connected to Antarctica and Australia during the Mesozoic as the coastal section of a continental-oceanic convergent boundary (Mortimer et al., 1999, 2017). The

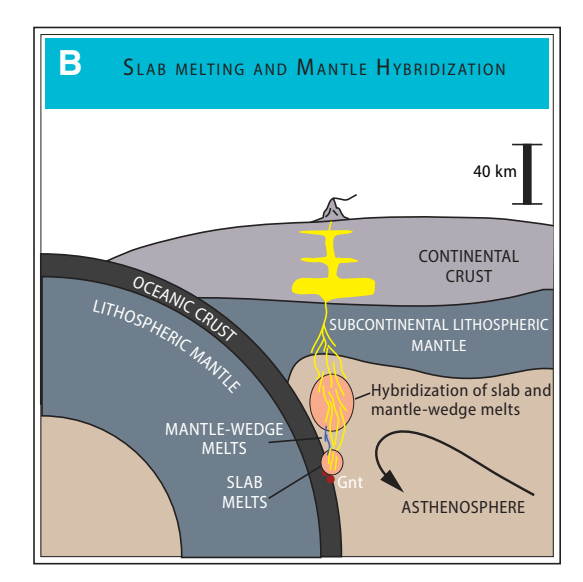
Median batholith in Fiordland is a composite suite of plutonic rocks covering >10,000 km² and preserves a record of Phanerozoic arc magmatism along the paleo-Pacific margin of southeastern Gondwana (Figs. 2A–2C) (Mortimer et al., 1999). The Median batholith separates accreted terranes of the Eastern province from Gondwana-affinity terranes of the Western province (Figs. 2B–2C).

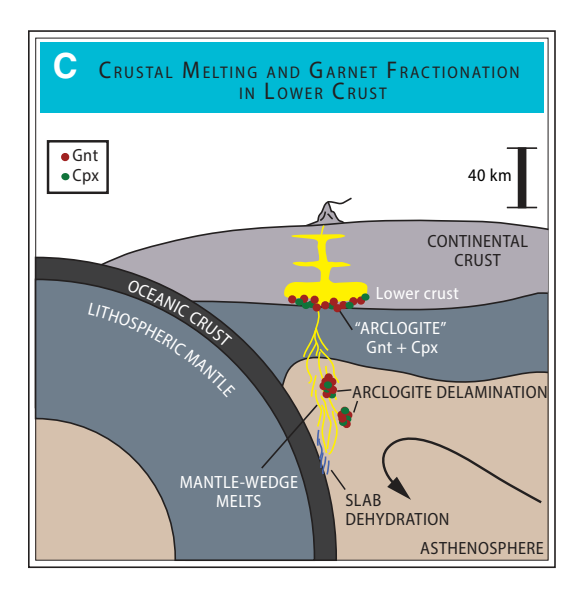
Tulloch and Kimbrough (2003) divided the Mesozoic phase of the Median batholith into an inboard, high-Sr/Y belt in the west and an outboard, low-Sr/Y belt in the east (Fig. 2A). The boundary between these belts is defined by a system of lower- to middle-crustal shear zones that were active in the Early Cretaceous (Indecision Creek and Grebe shear zones; Fig. 2A). The outboard belt consists of variously deformed and metamorphosed Triassic to Early Cretaceous plutonic rocks and represents a long-lived and relatively geographically stable subduction system (Tulloch and Kimbrough, 2003; Scott et al., 2011; Schwartz et al., 2021). The inboard belt consists of Early Cretaceous rocks that include lower-crustal diorites and monzodiorites of the Western Fiordland Orthogneiss (McCulloch et al., 1987) and shallow- to mid-crustal granites, granodiorites, and tonalites of the Separation Point Suite (Muir et al., 1995). Previous workers have argued that the high-Sr/Y signatures in both the Western Fiordland Orthogneiss and the Separation Point Suite reflect deep-crustal partial melting of a mafic arc root in the garnet stability field at depths >30 km, a model that we directly address in this study (Fig. 2C) (McCulloch et al., 1987; Muir et al., 1995; Daczko et al., 2001; Tulloch and Kimbrough, 2003; Scott et al., 2009; Chapman et al., 2017).

The Malaspina and Misty plutons represent two of the largest Early Cretaceous intrusive units of the Western Fiordland Orthogneiss (Fig. 3) (Allibone et al., 2009a). The plutons are similar in bulk-rock composition and consist of biotite-hornblende monzodiorites, hornblende-pyroxene monzodiorites, and pyroxene monzodiorites (Figs. 4A–4D) (Oliver, 1977, 1980; Klepeis et al., 2004, 2007; Allibone et al., 2009a). Zircon isotopic studies of the two plutons indicate that they have mantle-like  $\delta^{18}$ O (Zrn) values ranging from +5.2% to +6.3% and initial  $\epsilon_{\rm Hf}$  (Zrn) values ranging from –2.0 to +11.2 (Bolhar et al., 2008; Milan et al., 2016; Decker et al., 2017; Schwartz et al., 2021). Other Western Fiordland Orthogneiss plutonic rocks have bulk-rock initial  $\epsilon^{17}$ Sr/86Sr values of 0.70391  $\pm$  0.00004 and initial  $\epsilon_{\rm Nd}$  values ranging from –0.4 to +2.7 (McCulloch et al., 1987).

Studies of contact aureoles indicate that the Malaspina pluton was emplaced into the lower crust at >750 °C and 1.0–1.5 GPa (Allibone et al., 2009b). Al-inhornblende barometry of relict igneous amphiboles in the Malaspina pluton give an average pressure of  $0.92 \pm 0.09$  GPa (Carty et al., 2021), which overlaps the low end of the contact-aureole estimates. There are no similar studies of the Misty pluton; however, Klepeis et al. (2007) suggested that the Misty pluton may have structurally overlain the Malaspina pluton prior to Late Cretaceous extension in the arc starting at ca. 108–106 Ma (Klepeis et al., 2016; Schwartz et al., 2016). Both plutons were emplaced mostly at ca. 118–115 Ma during a brief, ~20 m.y. "flareup" of high-Sr/Y (>40) plutonic rocks (Milan et al., 2017; Schwartz et al., 2017, 2021; Ringwood et al., 2021). The flareup event involved abrupt widening and continentward (westward) migration of the Early Cretaceous arc axis and was immediately followed by high-grade metamorphism that was highly heterogeneous spatially (Oliver, 1980; Flowers et al., 2005; Klepeis







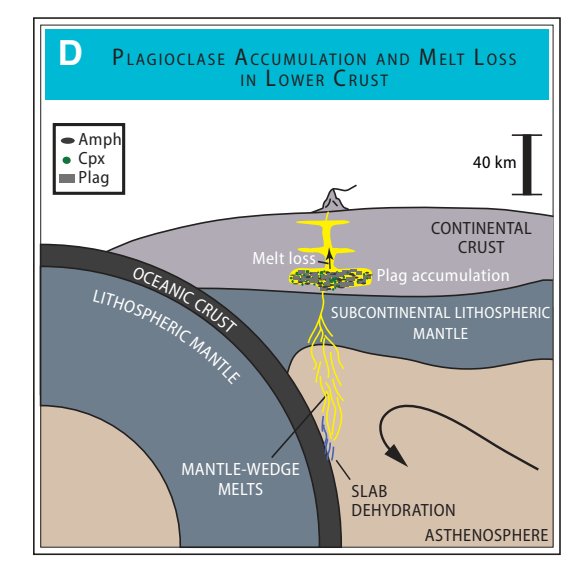


Figure 1. Cartoon diagrams of the various petrogenetic processes and mantle-crustal source compositions that can produce high-Sr/Y rocks in cordilleran arcs. Emphasis is on lower-crustal processes in a transcrustal melt system. (A) Slab-melting scenario involving partial melting of an eclogitic oceanic crust (e.g., Defant and Drummond, 1990). This scenario produces high-Sr/Y and high-SiO<sub>2</sub> melts. (B) Slab melts produced from melting of eclogitic oceanic crust hybridizing with hydrous mantle-wedge melts (e.g., Yogodzinski and Kelemen, 1998). This scenario produces high-Sr/Y melts with low SiO<sub>2</sub> contents similar to those found in the Western Fiordland Orthogneiss of Fiordland, New Zealand. (C) Partial melting of lower crust in the garnet stability field and/or fractionation of igneous garnet producing high-Sr/Y intracrustal melts and a residual garnet-bearing root (e.g., Petford and Atherton, 1996). Intracrustal melts produced via this scenario are used in crustal-thickness calculations (Chapman et al., 2015; Profeta et al., 2015). In thick cordilleran arcs (>40 km), high-pressure crystallization of igneous garnet and pyroxenes may produce a dense "arclogite" assemblage. Density contrasts between the arclogite and surrounding mantle may result in delamination and partial melting of the arclogite. (D) Crystal accumulation and melt loss from crystal-rich mush zones in the lower crust (e.g., Turnbull et al., 2010; Laurent et al., 2020). In this scenario, high-Sr/Y bulk rocks are produced by accumulation of Sr-rich plagioclase and melt loss. The cumulate residue is enriched in Sr relative to the original melt, producing an arc root with high-Sr/Y plutonic rocks. This is the preferred model in this study for the production of the high-Sr/Y bulk-rock compositions in the Western Fiordland Orthogneiss. Gnt-garnet; Cpx-clinopyroxene; Amph-amphibole; Plag-plagioclase.

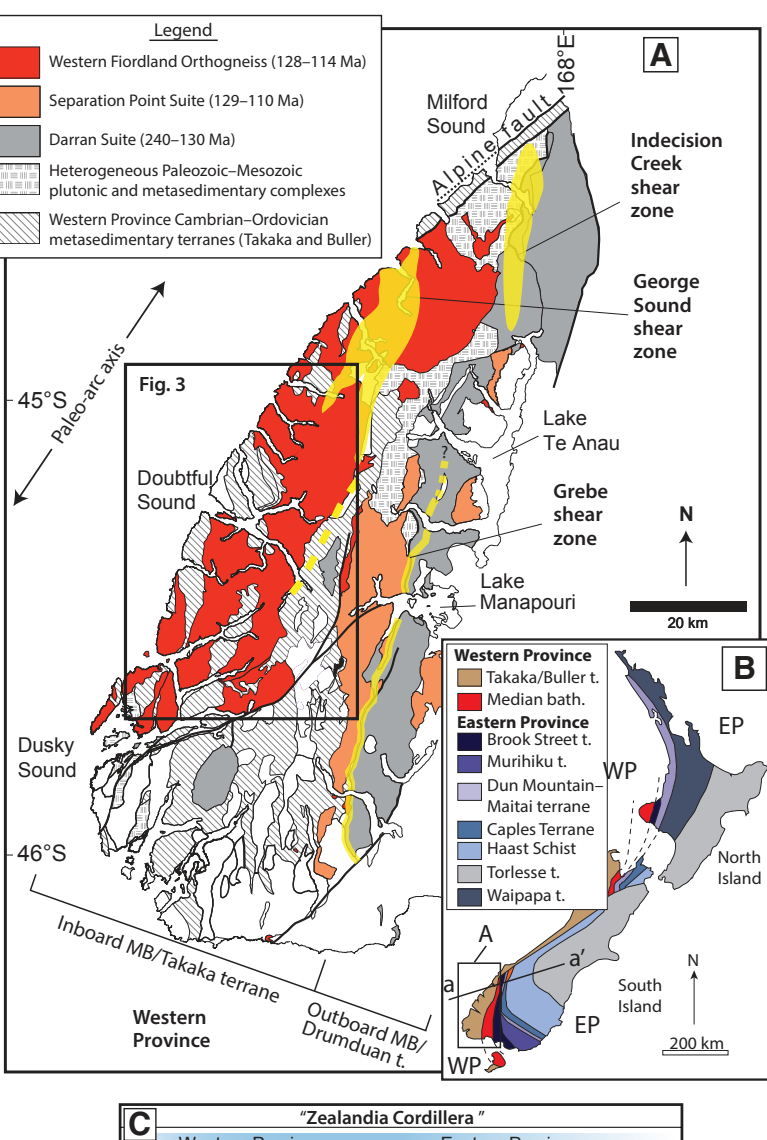
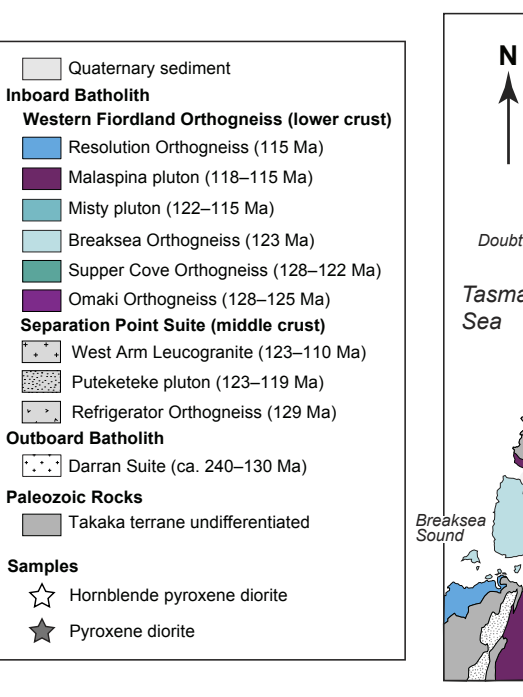


Figure 2. (A) Simplified geologic map of Fiordland, New Zealand, showing major intracrustal shear zones in yellow. The Grebe and Indecision Creek shear zones divide the inboard and outboard Median batholith. Black box indicates the study area and extent of Figure 3. Modified from Ramezani and Tulloch (2009). (B) Underlying basement terranes of present-day New Zealand. Dashed lines are extrapolations of terrane contacts. Line a-a' refers to the cross-section in C. Figure adapted from Coombs et al. (1976). (C) Simplified reconstructed cross-section of the Zealandia Cordillera showing the original emplacement of the Western Fiordland Orthogneiss (red) in the lower crust of the arc. Red, orange, and gray colors are the same as in A. Blue field indicates accreted terranes of the Eastern Province. Modified after Mortimer et al. (2014). MB-Median Batholith; EP-Eastern province; WP-Western province; t.-terrane; GSZ-Grebe shear zone; ICSZ-Indecision Creek shear zone; OB-outboard Median batholith; IB-inboard Median batholith.

Western Province Eastern Province a' a Median batholith Gondwana (km)20 km Buller Accreted terranes terrane Oceanic Subcontinental GSZ/ICSZ lithosphere This study



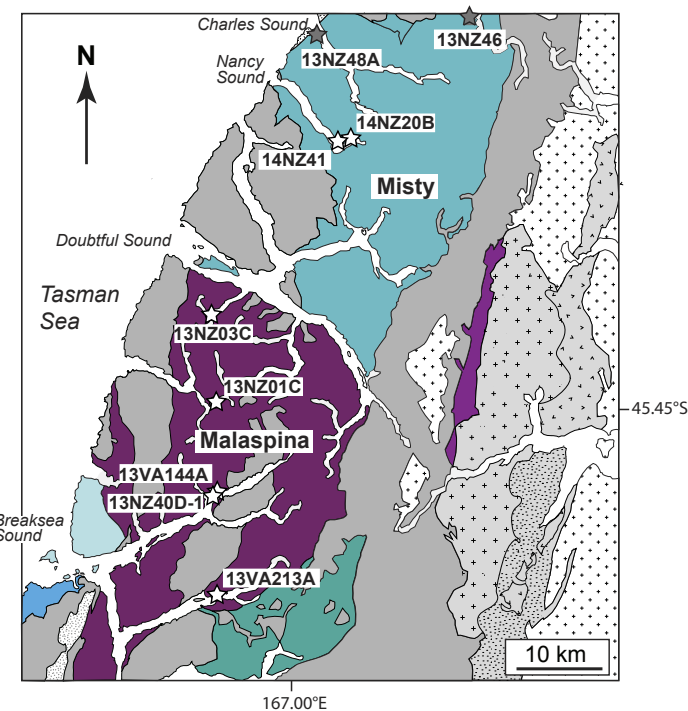


Figure 3. Geologic map of the southern extent of the Western Fiordland Orthogneiss showing sample locations in the Misty and Malaspina plutons. Modified after Stowell et al. (2014).

et al., 2007, 2016; De Paoli et al., 2009; Clarke et al., 2013; Stowell et al., 2014, 2017; Milan et al., 2017; Schwartz et al., 2017, 2021). Relict igneous assemblages are commonly preserved in both plutons and represent ideal opportunities to examine the significance of the Sr/Y geochemical signatures in lower-arc crust.

# METHODS

A total of nine clinopyroxene-bearing, high-Sr/Y plutonic rocks were collected on South Island, New Zealand, from the Malaspina and Misty plutons emplaced in the lower crust of the Median batholith (Table 1; Fig. 3). The study area covers >550 km² (Fig. 3), and samples are representative of the relict igneous assemblages found throughout the two plutons (Klepeis et al., 2016). Primary igneous textures are illustrated in Figure 5, and mineral assemblages are listed in Table 1.

# **Bulk-Rock Analysis**

Major elements and selected trace elements were determined for the nine samples by X-ray fluorescence (XRF; Table 2) at the Pomona College

XRF laboratory (Claremont, California, USA). Methodology and error analysis closely follow methods in Lackey et al. (2012). Representative whole-rock powders were prepared in an aluminum ceramic head and mill. Powdered sample and flux were mixed in a 1:2 ratio, typically 3.5 g powder to 7.0 g dilithium tetraborate (Li<sub>2</sub>B<sub>4</sub>O<sub>7</sub>). The vortexer-blended mixture was fused to a glass bead in a graphite crucible at 1000 °C for 10 min, reground, fused a second time, polished on diamond laps, and analyzed. The Pomona College laboratory analyzes major, minor, and 18 trace elements (Ba, Ce, Cr, Cu, Ga, La, Nb, Ni, Pb, Rb, Sc, Sr, Th, U, V, Y, Zn, Zr) on the same fused bead using a 3.0 kW Panalytical Axios wavelength-dispersive XRF spectrometer equipped with PE, LiF 200, LiF 220, GE, and PX1 industrial crystals. Concentrations are determined using reference calibration curves defined by 55 certified reference materials that span a range of natural igneous, metamorphic, and sedimentary rock compositions.

# **Clinopyroxene Major-Element Analysis**

Electron probe microanalyzer (EPMA) analysis was conducted at University of California, Los Angeles (UCLA), on a JEOL JXA-8200 Superprobe electron

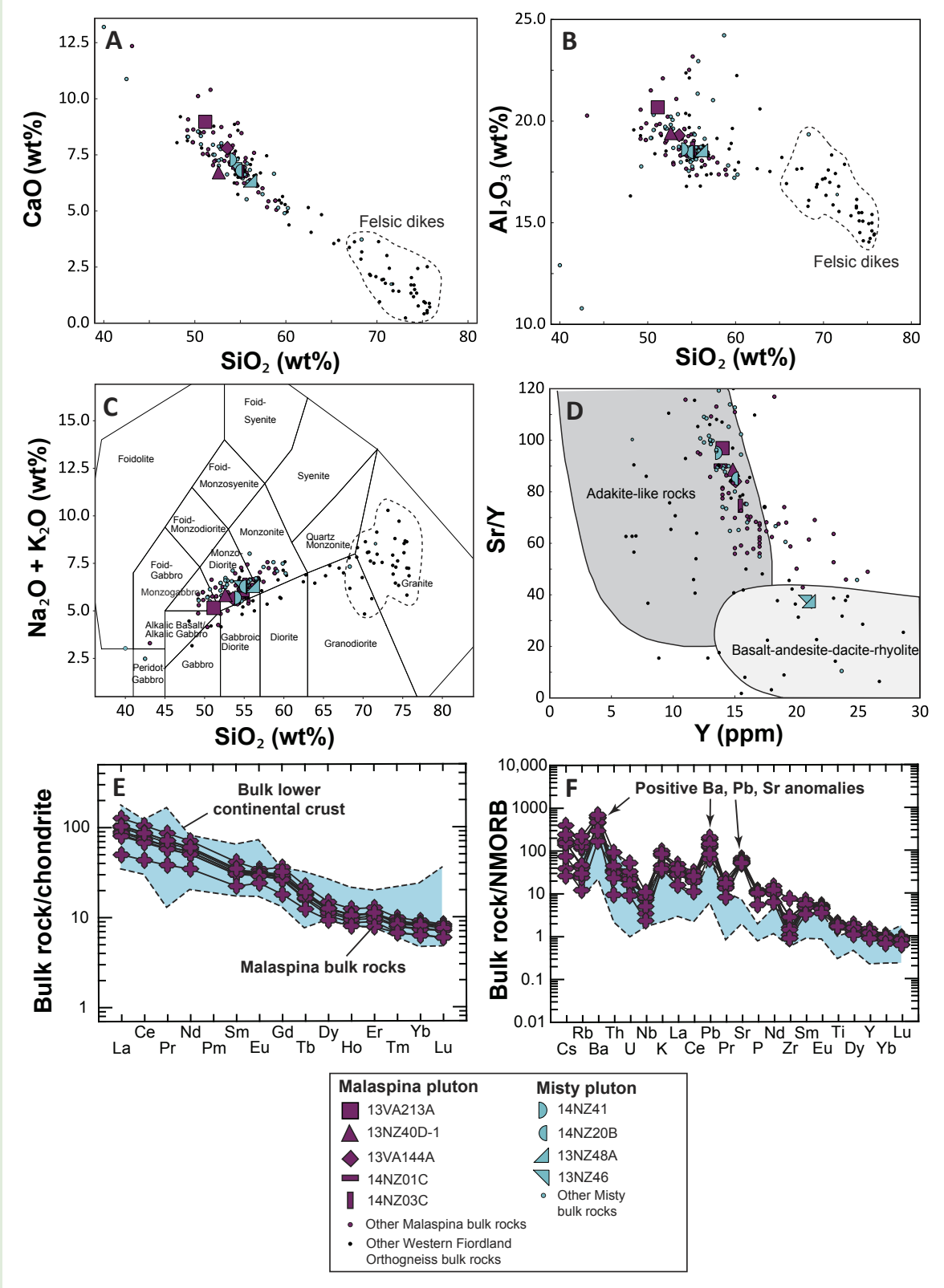


Figure 4. (A) SiO₂ versus CaO for X-ray fluorescence bulk-rock compositions of plutonic rocks showing Malaspina pluton samples in purple and Misty pluton samples in blue. Large symbols indicate samples with clinopyroxene analyses completed in this study. Additional data are from Decker et al. (2017). (B) SiO₂ versus Al₂O₃ for bulk-rock samples from Fiordland, New Zealand. (C) Total alkali–silica classification diagram. (D) Y versus Sr/Y for bulk-rock samples of the Western Fiordland Orthogneiss excluding felsic dikes. Most samples have high Sr/Y (≥40). (E) Chondrite-normalized rare-earth-element (REE) plots for the Malaspina pluton relative to bulk lower continental crust (blue). Malaspina pluton data show enriched light REE patterns and relatively flat heavy REE patterns. Chondrite-normalized plots were calculated using values from McDonough and Sun (1995). (F) Normal mid-ocean-ridge basalt (NMORB)–normalized trace-element variation patterns for the Malaspina pluton. Trace elements generally overlap lower-continental-crust estimates; however, elements compatible in plagioclase are particularly enriched in the Malaspina pluton (e.g., Ba, Pb, Sr). Bulk lower continental crust field is from Rudnick and Gao (2013).

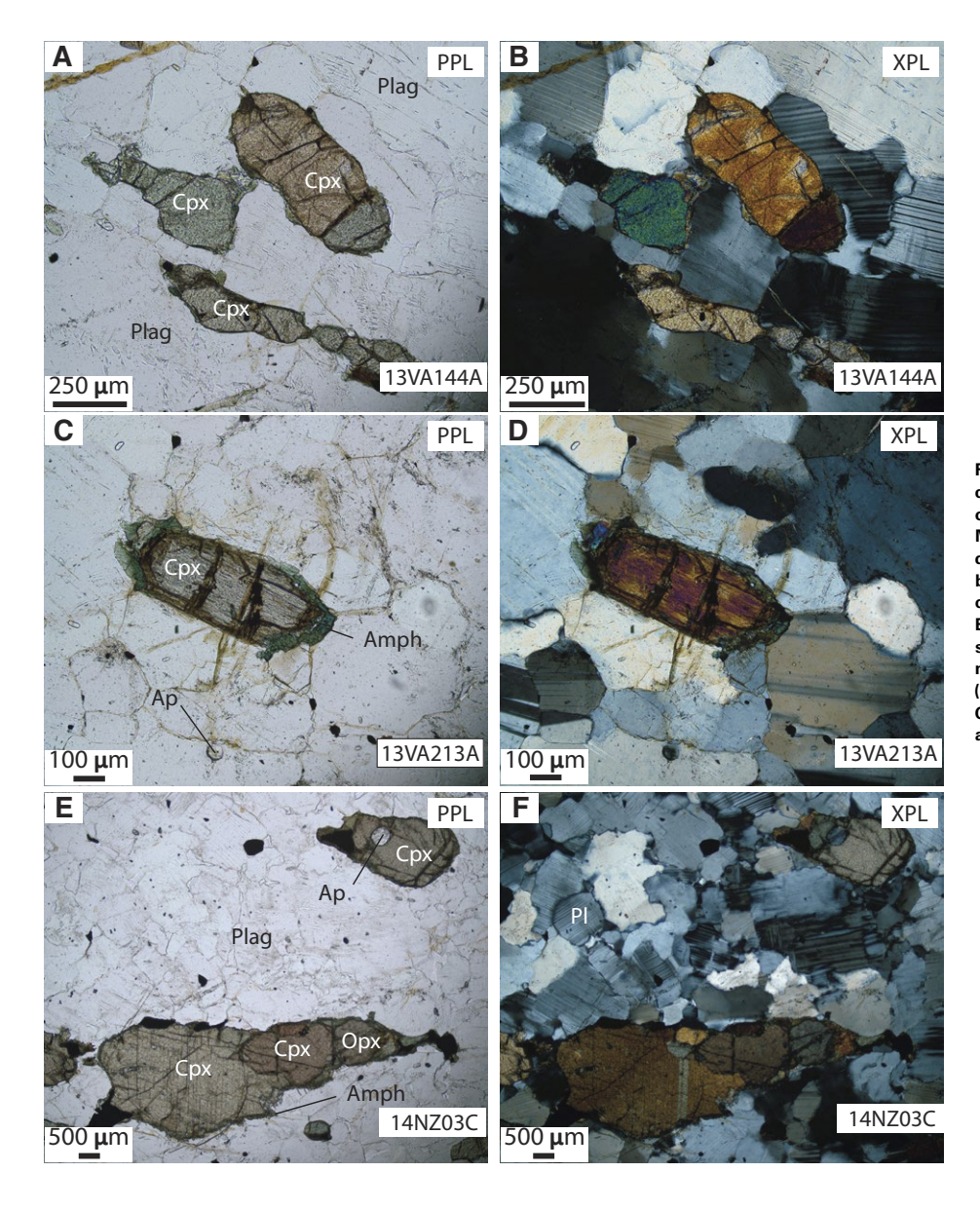


Figure 5. Plane-polarized light (PPL) and cross-polarized light (XPL) photomicrographs of magmatic clinopyroxene grains from the Malaspina pluton. (A–B) Subhedral to anhedral relict clinopyroxene crystals surrounded by plagioclase. Pyroxenes are free of inclusions or signs of post-emplacement alteration. (C–D) Euhedral igneous clinopyroxene grain with latestage amphibole rim. Small apatite crystals are notable within the surrounding plagioclase. (E–F) Large igneous clinopyroxene grains. Cpx—clinopyroxene; Plag—plagioclase; Amph—amphibole; Ap—apatite; Opx—orthopyroxene.

TABLE 1. LOCATION, ROCK TYPE, AND MAJOR MINERAL ASSEMBLAGES OF SAMPLES IN THIS STUDY

Sample				
number:	Latitude	Longitude	Rock type	Mineral assemblage
Malaspina plu	uton			
13VA144A	45°37′56.98″S	166°52′46.39″E	Hbl-Cpx diorite	Cpx, Opx, Plag, Ksp, Hbl, Bt, Ilm, Ap, Rt, Zrn
13VA213A	45°37′56.98″S	166°52′46.9″E	Hbl-Cpx diorite	Cpx, Opx, Plag, Ksp, Hbl, Bt, Ilm, Ap, Rt, Zrn
13NZ40D-1	45°32′58.77″S	166°51′12.19″E	Hbl-Cpx diorite	Cpx, Opx, Plag, Ksp, Hbl, Bt, Ilm, Ap, Rt, Zrn
14NZ01C	45°25′35.65″S	166°54′26.97"E	Hbl-Cpx diorite	Cpx, Opx, Plag, Ksp, Hbl, Bt, Ilm, Ap, Rt, Zrn
14NZ03C	45°20′21.38″S	166°54′10.88″E	Hbl-Cpx diorite	Cpx, Opx, Plag, Ksp, Hbl, Bt, Ilm, Ap, Rt, Zrn
Misty pluton				
13NZ48A	45°3′30.35″S	167°5′10.28″E	Hbl-Cpx diorite	Cpx, Opx, Plag, Ksp, Hbl, Ilm, Ap, Rt
13NZ46	45°2′39.09"S	167°17′24.63″E	Hbl-Cpx diorite	Cpx, Opx, Plag, Ksp, Hbl, Ilm, Rt, Ap, Zrn
14NZ20B	45°10′32.03″S	167°7′59.77″E	Hbl-Cpx diorite	Cpx, Opx, Plag, Ksp, Hbl, Ilm Ap, Zrn
14NZ41	45°8′23.06″S	167°9′11.79″E	Hbl-Cpx diorite	Cpx, Opx, Plag, Ksp, Hbl, Ilm, Ap, Zrn

Note: Cpx—clinopyroxene; Opx—orthopyroxene; Plag—plagioclase feldspar; Ksp—potassium feldspar; Hbl—hornblende; Bt—biotite; Ilm—ilmenite; Ap—apatite; Rt—rutile; Zrn—zircon.

TABLE 2. BULK-ROCK X-RAY FLUORESCENCE ANALYSES FOR SAMPLES FROM THE MALASPINA AND MISTY PLUTONS

Sample		Ма	laspina plutor	Misty pluton					
number:	13VA144A	13VA213A	13NZ40D-1	14NZ01C	14NZ03C	13NZ48A	13NZ46	14NZ20B	14NZ41
SiO <sub>2</sub>	53.49	51.14	52.59	54.78	55.11	56.08	54.45	54.82	54.22
$Al_2O_3$	19.33	20.68	19.43	18.39	18.65	18.57	18.45	18.48	18.61
TiO <sub>2</sub>	1.10	1.03	1.03	1.03	1.07	0.970	1.04	1.04	1.04
Fe <sub>2</sub> O <sub>3</sub>	8.03	7.56	9.78	8.45	7.93	7.52	8.80	8.29	8.44
MgO	3.71	4.72	3.99	4.00	3.58	3.65	3.66	3.71	4.18
MnO	0.13	0.07	0.14	0.13	0.12	0.11	0.12	0.13	0.13
CaO	7.83	8.97	6.74	6.95	6.76	6.36	6.86	6.80	7.28
K₂O	1.28	0.610	0.820	1.22	1.44	1.39	1.55	1.33	1.07
Na <sub>2</sub> O	4.41	4.55	5.04	4.65	4.93	4.93	4.68	4.95	4.62
Total	99.31	99.33	99.56	99.60	99.59	99.58	99.61	99.55	99.59
Mg#	47.8	55.3	44.7	48.4	47.2	49.0	45.2	47.0	49.5
Sr/Y	84	97	89	90	75	38	37	85	95

Note:  $Mg# = 100 \times Mg/(Mg + Fe)$ .

microprobe. Conditions were: 15kV accelerating voltage, 15 nA current, and a 5 µm beam. We used matrix-matched natural standards, and microprobe data were corrected using the ZAF (Atomic number, absorption, and fluorescence) correction scheme using coefficients from the FFAST database (Chantler et al., 2005). Structural formulae were calculated on the basis of six oxygen atoms. Representative clinopyroxene data are illustrated in Table 3, and all data are included in the Supplemental Material<sup>1</sup>.

# **Clinopyroxene Trace-Element Analysis**

Each spot analyzed by EPMA was also analyzed by in situ laser-ablation-sector-field-inductively coupled plasma mass spectrometry (LA-SF-ICPMS) for trace elements. Analyses were performed on a Teledyne Cetec Analyte G2 193 nm Excimer laser system paired with a Thermo Scientific Element2 high-resolution sector field ICPMS in the Department of Geological Sciences Laser Ablation Laboratory at California State University, Northridge. Ablation was conducted in a helium-atmosphere dual-volume cell. We conducted a blank run lasting ~20 min at the beginning of each day to permit background noise to reach a low baseline. Analyses of clinopyroxene were carried out using a

<sup>&</sup>lt;sup>1</sup>Supplemental Material. Bulk-rock and mineral geochemical data. Please visit <a href="https://doi.org/10.1130/GEOS.S.16926751">https://doi.org/10.1130/GEOS.S.16926751</a> to access the supplemental material, and contact editing @geosociety .org with any questions.

TABLE 3. REPRESENTATIVE CLINOPYROXENE COMPOSITIONS FOR THE MALASPINA AND MISTY PLUTONS

		Misty pluton							
Sample number:	13VA144A	13VA213A	13NZ40D-1	14NZ01C	14NZ03C	13NZ48A	13NZ46	14NZ20B	14NZ41
	Grain 2, spot 6	Grain 1, spot 14	Grain 2, spot 6	Grain 1, spot 6	Grain 1, spot 1	Grain 4, spot 23	Grain 1, spot 6	Grain 4, spot 21	Grain 1, spot 3
SiO <sub>2</sub>	48.31	51.40	51.39	51.58	50.29	50.07	50.47	50.17	49.66
$Al_2O_3$	7.98	3.89	3.96	4.30	6.17	6.38	4.78	5.44	5.60
TiO <sub>2</sub>	0.569	0.257	0.249	0.305	0.467	0.454	0.424	0.325	0.409
Cr <sub>2</sub> O <sub>3</sub>	_	_	_	0.064	0.067	0.002	_	_	_
Fe <sub>2</sub> O <sub>3</sub>	_	_	_	_	_	_	_	_	_
FeO	9.820	10.17	10.04	9.690	10.57	9.940	10.65	10.40	11.03
MgO	9.980	11.94	11.58	12.20	11.12	10.60	10.95	11.15	11.01
MnO	0.267	0.340	0.350	0.275	0.345	0.253	0.264	0.359	0.269
CaO	20.12	20.77	19.65	21.07	20.66	19.50	19.89	20.07	19.70
K₂O	0.022	0.010	0.011	0.002	0.038	0.003	_	_	0.027
Na₂O	1.59	1.37	1.70	1.34	1.44	1.68	1.25	1.52	1.56
Total	98.66	100.1	98.93	100.8	101.2	98.88	98.68	99.43	99.27
Mg#	64.4	67.7	67.3	69.2	65.2	65.5	64.7	65.6	64.0
Cations									
Si	1.821	1.909	1.929	1.899	1.851	1.882	1.912	1.877	1.863
Al	0.354	0.170	0.175	0.187	0.268	0.283	0.213	0.240	0.248
Ti	0.016	0.007	0.007	0.008	0.013	0.013	0.012	0.009	0.012
Cr	_	_	_	0.002	0.002	0.000	_	_	_
Fe <sup>2+</sup>	0.221	0.220	0.238	0.207	0.219	0.262	0.306	0.228	0.229
Fe <sup>3+</sup>	0.089	0.096	0.077	0.092	0.106	0.050	0.031	0.098	0.117
Mn	0.009	0.011	0.011	0.009	0.011	0.008	0.008	0.011	0.009
Mg	0.561	0.661	0.648	0.67	0.61	0.594	0.618	0.622	0.616
Ca	0.813	0.827	0.79	0.831	0.815	0.785	0.807	0.805	0.792
Na	0.116	0.099	0.124	0.096	0.103	0.122	0.092	0.110	0.113
K	0.001	0.000	0.001	0.000	0.002	0.000	0.000	0.000	0.001
Total	4.00	4.00	4.00	4.00	4.00	4.00	4.00	4.00	4.00

Note: Oxide concentrations are given in weight percent. Mg# = 100 × Mg/(Mg + Fe). Fe³+ estimated from stoichiometry. Dash indicates not analyzed. See the Supplemental Material (text footnote 1) for additional chemical analyses.

fluence of  $5.37 \text{ J/cm}^2$  at a pulse rate of 10 Hz and a beam diameter of  $50 \mu m$ . For each analysis, we recorded 20–30 s of background (laser off) and 60 s of signal, in addition to 60 s of background recorded at the beginning and end of each  $\sim$ 40 min run. We analyzed BHVO-2G (the primary standard) at the beginning, middle, and end of each run, as well as secondary analytical standards, BCR-2G and GSC-1G, at the beginning and end of each run.

Trace-element data were reduced using Iolite software (Paton et al., 2011), and weight percent CaO as determined by EMPA was used as an internal standard. We determined precision by repeated analysis of basaltic glass BHVO-2G. Long-term precision ranges from 3.2% to 15.9% for all analyzed elements excluding Cr and P. Accuracy as measured for basaltic glass BCR-2G was less than 5% for Ce, Er, Sm, Dy, Nd, V, Yb, Hf, Rb, Eu, Ho, Ta, Pr, Lu, Tb, La, Ti, Zr, Th, Gd, Y, Nb, Sc, Tm, P, and Zn and 10% for Mn, Ba, Sr, and U. Analyses of Ni and Pb were 12% and 13% low, respectively, compared to accepted values.

Cu was routinely 19% low and Cr 14% high, compared to accepted values of BCR-2G. Accuracy as measured for synthetic glass GSC-1G was better than 5% for Pb, Tb, Zn, Th, Ni, Gd, Er, Hf, Zr, Rb, Eu, Ho, Dy, Yb, Sr, Sm, Ba, and Nd, and 10% for V, Mn, U, La, Lu, Y, Pr, Cu, Ce, Tm, and Ti. Analyses of Ta and Nb were routinely >10% high, P and Cr were >20% high, compared to accepted values of BCR-2G. Representative LA-SF-ICPMS data are included in Table 4, and all data including standard information are contained in the Supplemental Material.

# Clinopyroxene Thermometry and Barometry

We calculated crystallization temperatures, pressures, and Fe-Mg exchange coefficients for clinopyroxenes after Putirka (2008) and Neave and Putirka

TABLE 4. REPRESENTATIVE PYROXENE TRACE-ELEMENT CONCENTRATIONS FOR THE MALASPINA AND MISTY PLUTONS

		N	lalaspina pluto	Misty pluton					
Sample number:	13VA144A	13VA213A Grain 1, spot 14	13NZ40D-1 Grain 2, spot 6	14NZ01C Grain 1, spot 6	14NZ03C Grain 1, spot 1	13NZ48A	13NZ46 Grain 1, spot 6	14NZ20B Grain 4, spot 21	14NZ41 Grain 1, spot 3
	Grain 2, spot 6					Grain 4, spot 23			
Rb	0.820	0.205	0.050	0.012	1.89	0.213	0.320	0.273	32.8
Sr	52.5	50.7	69.0	35.0	47.3	65.4	59.6	52.6	316
Υ	77.1	65.1	54.7	25.4	97.2	78.0	82.0	59.8	193
Zr	149	113	78.6	28.8	158	205	155	108	198
Nb	0.240	0.068	0.067	0.032	0.251	0.149	0.149	0.145	28.9
Ba	19.7	0.197	1.40	0.117	7.67	0.370	0.570	1.61	750
La	11.8	10.3	10.6	22.0	13.8	12.7	15.7	10.9	47.2
Ce	60.2	47.1	46.8	56.0	71.5	62.1	71.8	53.1	198
Pr	11.7	9.10	9.70	8.40	14.0	12.0	15.4	9.8	39.3
Nd	61.1	46.9	44.7	38.0	71.3	60.4	66.9	55.7	180
Sm	17.4	13.3	12.5	7.70	20.8	17.6	21.2	13.1	41.4
Eu	3.8	2.49	2.39	1.32	3.45	3.67	2.96	2.69	9.62
Gd	16.5	12.2	10.7	8.40	18.5	16.8	18.7	12.3	48.9
Tb	2.63	2.19	1.78	0.97	2.83	2.47	2.90	1.85	6.52
Dy	14.2	12.47	10.6	5.06	17.3	14.7	17.6	11.8	36.5
Ho	3.09	2.50	1.73	0.91	3.61	2.56	3.6	2.18	7.44
Er	7.98	6.87	4.87	2.54	9.80	7.22	9.80	6.20	17.2
Tm	1.15	0.972	0.680	0.353	1.45	1.11	1.39	0.930	3.08
Yb	7.37	5.86	4.00	2.01	8.25	6.30	8.60	5.50	15.3
Lu	1.07	1.01	0.679	0.292	1.33	0.909	1.36	0.75	2.03
Hf	6.20	5.06	3.36	1.18	6.01	7.70	6.70	4.60	7.49
Та	0.055	0.020	0.014	0.007	0.060	0.038	0.03	0.026	1.09
Pb	0.755	0.763	0.772	0.266	1.20	0.539	0.910	0.690	6.22
Th	0.523	0.640	0.530	1.17	0.610	0.640	0.560	0.172	0.770
U	0.082	0.051	0.160	0.320	0.217	0.068	0.129	0.046	0.143
Eu/Eu*	0.68	0.60	0.63	0.50	0.54	0.65	0.45	0.65	0.65
Sr/Y	0.68	0.78	1.3	1.4	0.49	0.84	0.73	0.88	1.6

Note: Trace-element concentrations are given in parts per million. Eu/Eu\* = (Eu)N[(Sm)N x (Gd)N]0.5.

(2017). We used the globally calibrated Jd-DiHd (Jadite [Jd], diopsdie [Di], hedenbergite [Hd]) exchange thermometer as published in Putirka (2008) to calculate temperatures of crystallization. The Putirka (2008) thermobarometer requires knowledge of a coexisting melt composition, and so we evaluated two temperature models using (1) bulk-rock XRF data as a proxy for melt compositions, and (2) amphibole-equilibrium melts using the chemometric equations derived by Zhang et al. (2017) from coexisting igneous amphiboles in the same samples (Carty et al., 2021). Amphibole-equilibrium melts display a restricted range in SiO<sub>2</sub> values (<5 wt%) for any given individual sample, and so we approximated the composition of coexisting melts using the average values for each sample (see amphibole-equilibrium melt data in Carty et al. [2021]). Sensitivity tests using maximum and minimum values for amphibole-equilibrium melt compositions indicate an uncertainty of as much as

 $20~^\circ\text{C}$  for clinopyroxene crystallization temperatures based on uncertainties in coexisting amphibole-equilibrium melt compositions. We assumed both 3 wt% and 6 wt%  $\text{H}_2\text{O}$  based on the presence of magmatic amphibole to test the sensitivity of temperature models to water content. Calculated temperatures were tested for equilibrium between pyroxenes and assumed melts by examining calculated Fe-Mg exchange coefficients  $(K_{\text{D(Fe-Mg)}})$  and comparing data to the experimentally determined global range of 0.27  $\pm$  0.03 (Putirka, 2008). Fe-Mg exchange coefficients are calculated on an anhydrous basis following methods of Putirka (2008). Pressures were calculated using the jadeite-in-clinopyroxene barometer of Neave and Putirka (2017). This geobarometer has been experimentally calibrated from 0.001 to 20 kbar and 950 °C to 1400 °C and includes both hydrous and anhydrous samples. It is therefore appropriate to our study conditions and expected emplacement depths.

# **Partition Coefficients and Melt Calculations**

We calculated clinopyroxene-equilibrium melt concentrations using experimental partition coefficient values from a variety of studies. We primarily report calculated melts using values from Severs et al. (2009) established through LA-ICPMS studies of melt inclusions in volcanic rocks from New Zealand, though we also explore other partition coefficients for the purpose of sensitivity calculations (e.g., Luhr and Carmichael, 1980; Sisson, 1991; Ewart and Griffin, 1994; Blundy et al., 1998; Green et al., 2000; Wood and Trigila, 2001). Partition coefficients calculated by Severs et al. (2009) are based on an intermediate dacitic melt erupted on White Island, New Zealand. Malaspina and Misty pluton melts were also andesitic to dacitic in composition (see Carty et al., 2021), which makes the Severs et al. (2009) partition coefficients the most compositionally appropriate to our study. The other tested partition coefficients are based on a variety of laboratory-created and natural samples ranging from shallow (≤0.3 GPa) intermediate and felsic volcanic samples (Luhr and Carmichael, 1980; Ewart and Griffin, 1994; Wood and Trigila, 2001) to high-pressure (1.5+ GPa) experiments simulating melting of the mantle (Blundy et al., 1998; Green et al., 2000). This allows us to constrain the precision of our results,

and importantly, our resulting Sr/Y calculations are insensitive to selection of partition coefficients or pressure-temperature (*P-T*) conditions; therefore, variations in parental melt compositions do not modify any conclusions about the discrepancy between bulk-rock values and clinopyroxene–equilibrium melt compositions (see Table 5 and the Supplemental Material).

# RESULTS

# Petrography

Samples in this study range from hornblende-pyroxene monzodiorites to pyroxene monzodiorites (Table 2; Figs. 4A–4D). Common major igneous mineral assemblages include plagioclase, clinopyroxene, orthopyroxene, amphibole, biotite, potassium feldspar, and ilmenite ± zircon, apatite, and rutile (Table 1). All samples are hypidiomorphic and display moderate hypersolidus foliations, with notable alignment of mafic mineral assemblages (clinopyroxene, orthopyroxene, amphibole). Pyroxenes and amphiboles are generally inclusion free but in some cases have small apatite inclusions. Petrographic relationships

TABLE 5. CALCULATED MELT COMPOSITIONS USING VARIOUS CLINOPYROXENE TRACE-ELEMENT PARTITION COEFFICIENTS

	М	alaspina pluton	Misty pluton					
13VA144A Grain 2, spot 6	13VA213A Grain 1, spot 14	13NZ40D-1 Grain 2, spot 6	14NZ01C Grain 1, spot 6	14NZ03C Grain 1, spot 1	13NZ48A Grain 4, spot 23	13NZ46 Grain 1, spot 6	14NZ20B Grain 4, spot 21	14NZ41 Grain 1, spot 3
519.0 81.0	502.0 69.0	683.0 58.0	347.0 27.0	468.0 102	648.0 82.0	590.0 86.0	425.0 54.0	3129 203
0.80 6.4	0.71 7.3	0.75 12	0.60 13	0.64 4.6	0.78 7.9	0.54 6.8	979.0 0.88 7.8	2041 0.78 15
3)								
846.8 60.7 552 1.4 13.9	817.7 51.3 418 1.3 16.0	1113 43.1 291 1.3 25.8	564.5 20.0 107 1.1 28.2	762.9 76.5 585 1.2 10.0	1055 61.4 759 1.4 17.2	961.3 64.6 574 0.97 14.9	691.9 40.5 352 1.6 17.1	5097 152 733 1.4 33.5
1994)								
187.5 32 452 n.d.	181.1 27 342 n.d.	246.4 23 238 n.d.	125.0 11 87.3 n.d.	168.9 41 479 n.d.	233.6 33 621 n.d.	212.9 34 470 n.d.	153.2 21 288 n.d.	1129 80 600 n.d. 14
	Grain 2, spot 6  ) 519.0 81.0 1537 0.80 6.4 ) 846.8 60.7 552 1.4 13.9 1994) 187.5 32 452	13VA144A 13VA213A  Grain 2, Grain 1, spot 6 502.0  81.0 69.0 1537 1163 0.80 0.71 6.4 7.3  )  846.8 817.7 60.7 51.3 552 418 1.4 1.3 13.9 16.0 1994) 187.5 181.1 32 27 452 342 n.d. n.d.	13VA144A 13VA213A 13NZ40D-1  Grain 2, spot 6 spot 14 spot 6   519.0 502.0 683.0 81.0 69.0 58.0 1537 1163 510.0 0.75 6.4 7.3 12   846.8 817.7 1113 60.7 51.3 43.1 552 418 291 1.4 1.3 1.3 13.9 16.0 25.8 1994)  187.5 181.1 246.4 32 27 23 452 342 238 n.d. n.d. n.d.	Grain 2, spot 6 Spot 14 Spot 6 Spot 6    Spot 6 Spot 14 Spot 6 Sp	13VA144A	13VA144A         13VA213A         13NZ40D-1         14NZ01C         14NZ03C         13NZ48A           Grain 2, spot 6         Grain 1, spot 6         Grain 1, spot 6         Grain 1, spot 1         Grain 1, spot 1         Grain 1, spot 23           1         519.0         502.0         683.0         347.0         468.0         648.0           81.0         69.0         58.0         27.0         102         82.0           1537         1163         510.0         297.0         1629         2113           0.80         0.71         0.75         0.60         0.64         0.78           6.4         7.3         12         13         4.6         7.9           1         846.8         817.7         1113         564.5         762.9         1055           60.7         51.3         43.1         20.0         76.5         61.4           552         418         291         107         585         759           1.4         1.3         1.3         1.1         1.2         1.4           13.9         16.0         25.8         28.2         10.0         17.2           1994)         187.5         181.1         246.4         1	13VA144A	13VA144A

Note: Trace-element concentrations are given in parts per million are calculated using values from Severs et al. (2009), Blundy et al. (1998), and Ewart and Griffin (1994). Calculated Sr/Y is <40 regardless of choice of experimental coefficients. Eu/Eu\* = (Eu)N[(Sm)N x (Gd)N]0.5. n.d. indicates not determined.

suggest that the pyroxene and hornblende formed first, followed by crystallization of plagioclase. Pyroxenes and hornblende are typically subhedral and occur as glomerocrysts within a larger groundmass of interlocked anhedral plagioclase crystals (Figs. 5E–5F). Clinopyroxenes range from subhedral to euhedral. Orthopyroxenes typically display exsolution lamellae of clinopyroxene. Amphibole grains are commonly dark green in plane-polarized light, range from anhedral to subhedral, and in some cases display reaction rims of biotite. Plagioclase is generally anhedral to subhedral, and a few samples display sutured grain boundaries (Figs. 5E–5F). We do not observe any evidence of dynamic recrystallization of pyroxenes or amphiboles in these rocks.

#### **Bulk-Rock Geochemical Data**

Bulk-rock analysis of 72 rocks from the Malaspina pluton reveals an average  $SiO_2$  of 53.9 wt% (Supplemental Material) with the five rocks in this study ranging from 51.1 to 55.1 wt% (Fig. 4; Table 2; Supplemental Material). Four samples have molar Mg# [100 × Mg/(Mg + Fe)] values ranging from 44.7 to 48.4 while one sample (13VA213A) has a molar Mg# of 55.3 (mean = 48.7,  $2\sigma$  = 8). Al $_2O_3$  ranges from 18.4 to 20.7 wt% (mean = 19.3,  $2\sigma$  = 2). K $_2O$  ranges from 0.61 to 1.44 wt% (mean = 1.1,  $2\sigma$  = 1). Na $_2O$  ranges from 4.41 to 5.04 wt% (mean = 4.7,  $2\sigma$  = 1). CaO ranges from 6.74 to 8.97 wt% (mean = 7.45,  $2\sigma$  = 2).

In the Misty pluton,  $SiO_2$  is more variable, ranging from 40.0 to 71.6 wt% in 52 rocks; Supplemental Material). The four samples in this study range from 54.2 to 56.1 wt% (mean = 54.9,  $2\sigma$  = 2) (Table 2). Mg# also varies significantly in the full data set, from a minimum of 28.9 up to 60.9. The Mg# of the samples analyzed from the Misty pluton for this study are similar to those from the Malaspina pluton and range from 45.2 to 49.5 (mean = 47.7,  $2\sigma$  = 8).

Bulk-rock samples are mostly classified as monzogabbro to monzonite with some late-stage dikes evolved enough to be categorized as granites (Fig. 4A). U-Pb zircon geochronology shows that the late-stage felsic dikes generally postdate Malaspina and Misty pluton crystallization and are not considered further in this study (Klepeis et al., 2007, 2016; Schwartz et al., 2017). Bulk-rock data in this study from the Malaspina pluton show Sr/Y values ranging from 74.6 to 96.9 (x = 86.9,  $2\sigma = 17$ ); samples from the Misty pluton are more variable, ranging from 37.3 to 95.1 (x = 63.8,  $2\sigma = 31$ ) (Fig. 4B). These results confirm data from prior studies in terms of bulk composition (cf. Tulloch and Kimbrough, 2003, for discussion of high Sr/Y values).

# Clinopyroxene Geochemical Data

# Major-Element Data

To classify pyroxenes, we normalized major elements to 100% and calculated end-member compositions as enstatite (En), ferrosilite (Fs), wollastonite (Wo), or where appropriate as aegerine (Aeg), jadite (Jd), and diopside (Di).

The majority of clinopyroxenes in this study are Ca-Mg-Fe ("quadrilateral") pyroxenes and have average end-member compositions of 37.8% En, 13.7% Fs, and 48.5% Wo in the Malaspina pluton and 38.1% En, 15.0% Fs, and 46.9% Wo in the Misty pluton. Ninety-four analyses have sufficient Na and Al to be classified according to the Aeg-Jd-Di classification (Morimoto, 1988) and have average compositions of 10.2% Aeg, 1.67% Jd, and 88.1% Di in the Malaspina pluton and 10.7% Aeg, 1.29% Jd, and 88.0% Di in the Misty pluton. Representative major-element analyses are shown in Table 3, and complete data are available in the Supplemental Material. Analyzed clinopyroxenes are shown on pyroxene classification diagrams in Figure 6.

In 136 analyzed spots across 23 clinopyroxene grains, molar Mg# ranges from 60.0 to 69.8 (mean = 65.8,  $2\sigma$  = 4). We use Mg# as an index of differentiation, based on the preferential partitioning of available Mg into ferromagnesian silicate minerals over melt causing a progressive decrease in Mg# during continued fractional crystallization in a closed system. Large core-to-rim variations are uncommon in our samples, but we do observe increases in FeO and decreases in Mg# in most analyzed grains. The major-oxide contents decrease monotonically and follow simple fractional crystallization trends in both the Misty and Malaspina plutons (Figs. 7A–7D). SiO<sub>2</sub> in clinopyroxene samples from the Malaspina pluton ranges from 48.0 to 52.5 wt% (x = 50.4,  $2\sigma$  = 2). Misty Pluton clinopyroxenes are identical to those in the Malaspina Pluton within error, with SiO<sub>2</sub> ranging from 49.7 to 51.0 wt% (x = 50.2,  $2\sigma$  = 3).

Sample 13VA144A deviates from other samples in the Malaspina Pluton in terms of  $Al_2O_3$  concentrations. While four samples record a steep increase in  $Al_2O_3$  with differentiation, sample 13VA144A has an initial  $Al_2O_3$  concentration higher than the final concentration of the other samples and a relatively flat trend (Fig. 7B). Samples in the Malaspina pluton with lower  $Al_2O_3$  have

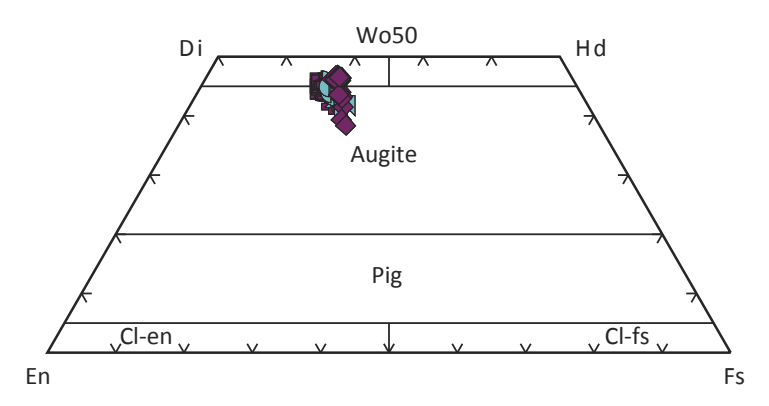


Figure 6. Pyroxene quadrilateral showing classification for all analyzed spots from the Malaspina and Misty plutons. Samples are mostly diopside and augite. Blue symbols are Misty pluton clinopyroxenes, and purple symbols are Malaspina pluton clinopyroxenes. En—enstatite; Fs—ferrosilite; Wo—wollastonite; Di—diopside; Hd—hedenbergite; Cl—clino-m; Pig—pigeonite.

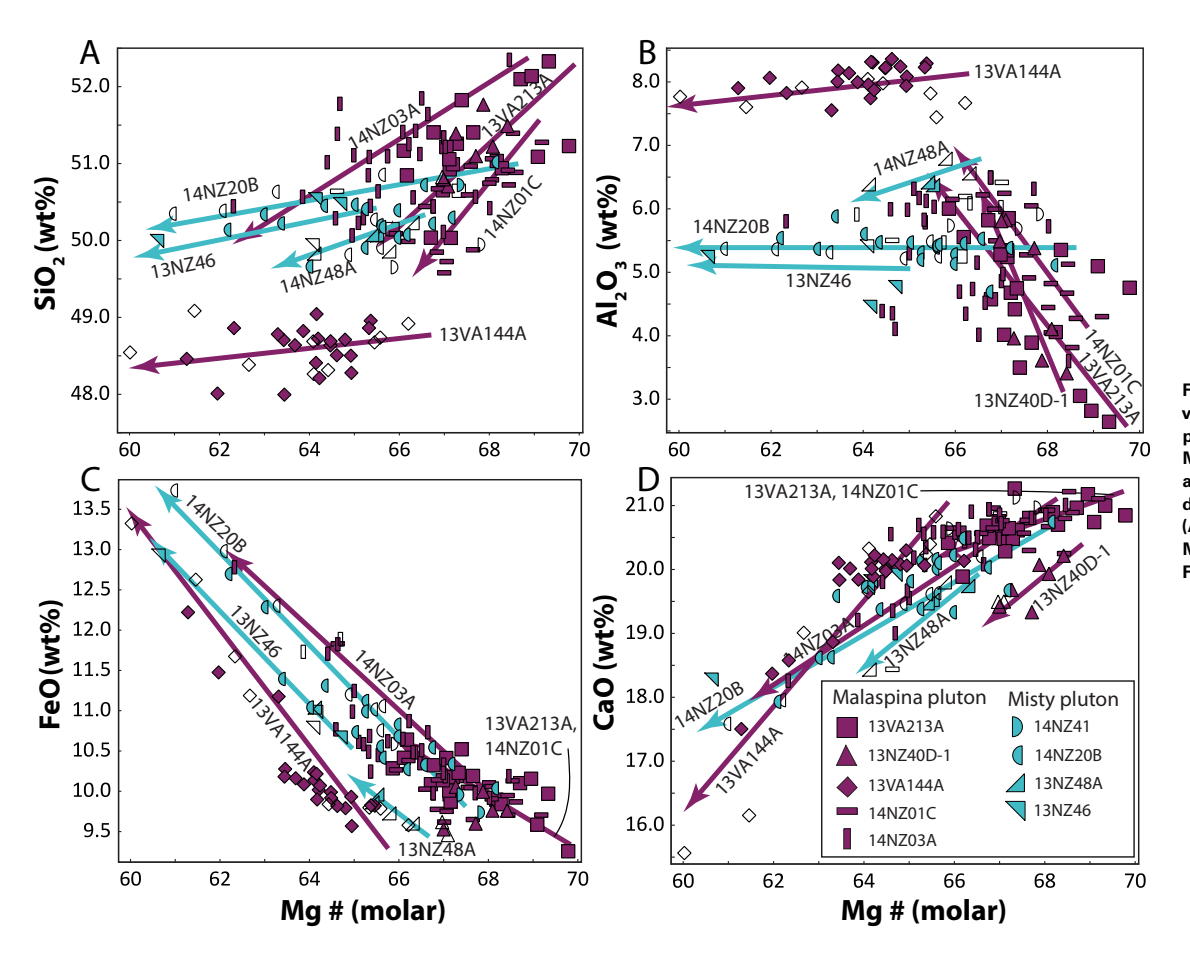


Figure 7. Molar Mg# [100 x Mg/(Mg + Fe)] versus major oxides for analyzed clinopyroxene grains from the Malaspina and Misty plutons. Hollow symbols are rim analyses. Colored arrows show general differentiation trends for each sample. (A) Molar Mg# versus SiO<sub>2</sub>. (B) Molar Mg# versus Al<sub>2</sub>O<sub>3</sub>. (C) Molar Mg# versus FeO. (D) Molar Mg# versus CaO.

concentrations ranging from 2.6 to 6.4 wt% (mean = 5.0,  $2\sigma$  = 2), while analyzed clinopyroxene spots in sample 13VA144A have a mean Al<sub>2</sub>O<sub>3</sub> concentration of 8.0 wt% ( $2\sigma$  = 0.5). The Misty pluton displays similar average concentrations to the Malaspina pluton with Al<sub>2</sub>O<sub>3</sub> ranging from 4.5 to 6.8 wt% (mean = 5.5,  $2\sigma$  = 1). CaO is correlated strongly with Mg# in both plutons and ranges from 17.6 to 21.3 wt% (mean = 20.3,  $2\sigma$  = 2) in the Malaspina pluton and 17.6 to 21.1 wt% (mean = 19.7,  $2\sigma$  = 2) in the Misty pluton (Fig. 7D).

# Trace-Element Data

Clinopyroxenes in the Malaspina pluton have low Sr concentrations that range from 1.5 to 89 ppm ( $x = 50.3, 2\sigma = 28$ ) (Supplemental File). Clinopyroxenes

from the Misty pluton have Sr concentrations similar to those from the Malaspina pluton, ranging from 36.7 to 83.0 (x = 49.6,  $2\sigma$  = 19) except for two outliers from the same grain in sample 14NZ41 with values of 267 ppm and 316 ppm (Fig. 8). Y concentrations range from 16.6 to 97.2 ppm and from 42.9 to 207 ppm in the Malaspina and Misty plutons, respectively (Fig. 9B). These values overlap those from clinopyroxenes from fractionated arc magmas rather than from high-Sr/Y adakites (Fig. 8).

High-field-strength element concentrations in clinopyroxenes from both plutons generally overlap and display similar trends when using Zr as an index of differentiation and progressive crystal growth (see core-to-rim arrows on Fig. 9). For example, Hf concentration ranges from 1.2 to 8.7 ppm (x = 4.9,  $\sigma = 1.4$ ) and is well correlated with Zr in all samples (Fig. 9A). Nb concentrations display a broad range from 0.03 to 29 ppm with a mean of 0.62 ppm ( $\sigma = 6$ )

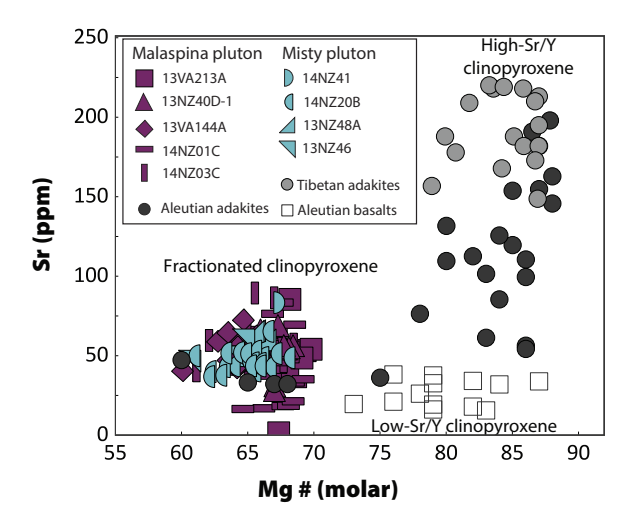


Figure 8. Molar Mg# [100 x Mg/(Mg + Fe)] versus Sr for Misty and Malaspina pluton clinopyroxenes. Colored symbols are analyses performed for this study. Two analyses from the Misty pluton have anomalously high Sr concentrations (267 ppm and 316 ppm; not shown) and low Sr/Y values similar to those of other analyses in this data set. Hollow squares are clinopyroxenes from Quaternary Aleutian basalts (Alaska, USA), and dark gray circles are clinopyroxenes from Cenozoic Aleutian adakites (Yogodzinski and Kelemen, 1998); light gray circles are high-Sr/Y clinopyroxene rims in Eocene adakites from the Tibetan Plateau (Zeng et al., 2020).

and covary with Zr (Fig. 9C). Ta concentrations range from 0.007 to 1.09 ppm (x = 0.1,  $\sigma = 0.2$ ) and covary with Zr (Fig. 9D). Overall, the nine samples show similar positively correlated trends in high-field-strength elements, apart from samples 13NZ40D-1 and 14NZ03A, which preserve more complex crystallization histories with bimodal distributions (Figs. 9B–9D). Notably, sample 13VA144A plots together with other samples in terms of high-field-strength elements despite displaying distinct SiO<sub>2</sub> and Al<sub>2</sub>O<sub>3</sub> concentrations.

Clinopyroxenes from the Malaspina and Misty plutons show increasing Sr/Y and decreasing Eu/Eu\* (Eu/Eu\* = (Eu)N[(Sm)N x (Gd)N]0.5) with decreasing Zr concentrations (Figs. 10A–10B). Sr/Y values in clinopyroxenes from the Malaspina and Misty plutons range from 0.47 to 1.8 and from 0.53 to 1.6, respectively. All clinopyroxenes display negative Eu anomalies (0.45  $\leq$  Eu/Eu\*  $\leq$  0.88) with weak decreasing trends with decreasing Zr concentrations (Fig. 10B).

All clinopyroxenes show a similar overall shape on chondrite-normalized rare-earth element (REE) diagrams and are enriched by 10x to >100x as compared to chondritic values (Fig. 11). They display prominent negative Eu anomalies as well as a "spoon-shaped" enrichment in light REEs. The bimodal distribution of sample 14NZ01C apparent in the bivariate trace-element plots (Figs. 9 and 10) is clearly demonstrated again here with two populations. Relative to clinopyroxenes in Aleutian adakites (Yogodzinski and Kelemen, 1998),

clinopyroxenes in this study are enriched in REEs but show similar overall patterns with the exception of pronounced Eu anomalies in our samples. Aleutian and Tibetan adakites have overlapping to higher Sm/Yb values, compared to the studied samples, and show steep trends in Sm/Yb versus Zr space indicative of garnet control (Yogodzinski and Kelemen, 1998; Zeng et al., 2020). In contrast, clinopyroxenes from the Malaspina and Misty plutons show subhorizontal trends that are consistent with plagioclase + clinopyroxene + amphibole fractionation (see "gabbro" control in Fig. 10C) (Davidson et al., 2007).

# Clinopyroxene Thermometry and Barometry

Using bulk-rock chemistry as a proxy for melt compositions results in calculated crystallization temperatures of 1098 °C to 1167 °C (x = 1126 °C,  $2\sigma$  = 35 °C) at 3 wt% H<sub>2</sub>O for the Malaspina pluton and 1090 °C to 1144 °C (x = 1118 °C,  $2\sigma$  = 28 °C) for the Misty pluton. Fe-Mg exchange coefficients ( $K_{\text{D(Fe-Mg)}}$ ) for this model yield average values of 0.48 ( $2\sigma$  = 0.09) and 0.43 ( $2\sigma$  = 0.03) for the Malaspina and Misty plutons, respectively, well outside the experimentally calibrated value of 0.27 ± 0.03 (Putirka, 2008). Using a higher water content of 6 wt% for these bulk rock–based models also results in deviation of  $K_{\text{D(Fe-Mg)}}$  from the accepted range ( $K_{\text{D(Fe-Mg)}}$  = 0.48 ± 0.09 in the Malaspina pluton;  $K_{\text{D(Fe-Mg)}}$  = 0.43 ± 0.03 in the Misty pluton) and slightly lower crystallization temperatures ranging from 1058 °C to 1121 °C (x = 1084 °C,  $2\sigma$  = 33 °C) for the Malaspina pluton and 1050 °C to 1100 °C (x = 1076 °C, x = 26 °C) for the Misty pluton.

Calculated clinopyroxene temperatures using amphibole-equilibrium melts and 3 wt% H<sub>2</sub>O range from 1035 °C to 1081 °C (x = 1054 °C,  $2\sigma$  = 20 °C;) and 1050 °C to 1087 °C (x = 1066 °C,  $2\sigma$  = 19 °C) for the Malaspina and Misty plutons, respectively. At 6 wt% H<sub>2</sub>O, crystallization temperatures in the Malaspina pluton range from 986 °C to 1051 °C (x = 1009 °C,  $2\sigma$  = 30 °C) and calculated temperatures in the Misty pluton range from 1006 °C to 1041 °C (x = 1021 °C,  $2\sigma$  = 18 °C). K<sub>D(Fe-Mg)</sub> values for these models are 0.25 ± 0.04 and 0.27 ± 0.04 in the Malaspina and Misty plutons, respectively, values that overlap experimentally calibrated values, indicating that these models are viable though nonunique solutions.

Using the jadeite-in-clinopyroxene geobarometer from Neave and Putirka (2017), we also calculated crystallization pressures for bulk-rock and calculated equlibrium melt models with 3 and 6 wt% water. Bulk-rock XRF-based models produce pressures averaging 1.23 GPa ( $2\sigma$  = 0.2 GPa) in the Malaspina pluton and 1.23 GPa ( $2\sigma$  = 0.1 GPa) in the Misty pluton at 3 wt% H<sub>2</sub>O. Increased water content of 6 wt% reduces these average pressures to 1.18 GPa ( $2\sigma$  = 0.2 GPa) and 1.18 GPa ( $2\sigma$  = 0.1 GPa) in the Malaspina and Misty plutons, respectively.

Clinopyroxene crystallization pressures calculated using melt compositions from coexisting hornblendes are 1.09 GPa at 3 wt%  $H_2O$  ( $2\sigma=0.1$  GPa) and 0.95 GPa at 6 wt%  $H_2O$  ( $2\sigma=0.1$  GPa) in the Malaspina pluton, and 1.14 GPa at 3 wt%  $H_2O$  ( $2\sigma=0.04$  GPa) and 1.02 GPa at 6 wt%  $H_2O$  ( $2\sigma=0.04$  GPa) in the Misty pluton. All models fall within the 0.14 GPa standard error of the jadeite-in-clinopyroxene barometer as determined by Neave and Putirka (2017) (1.09

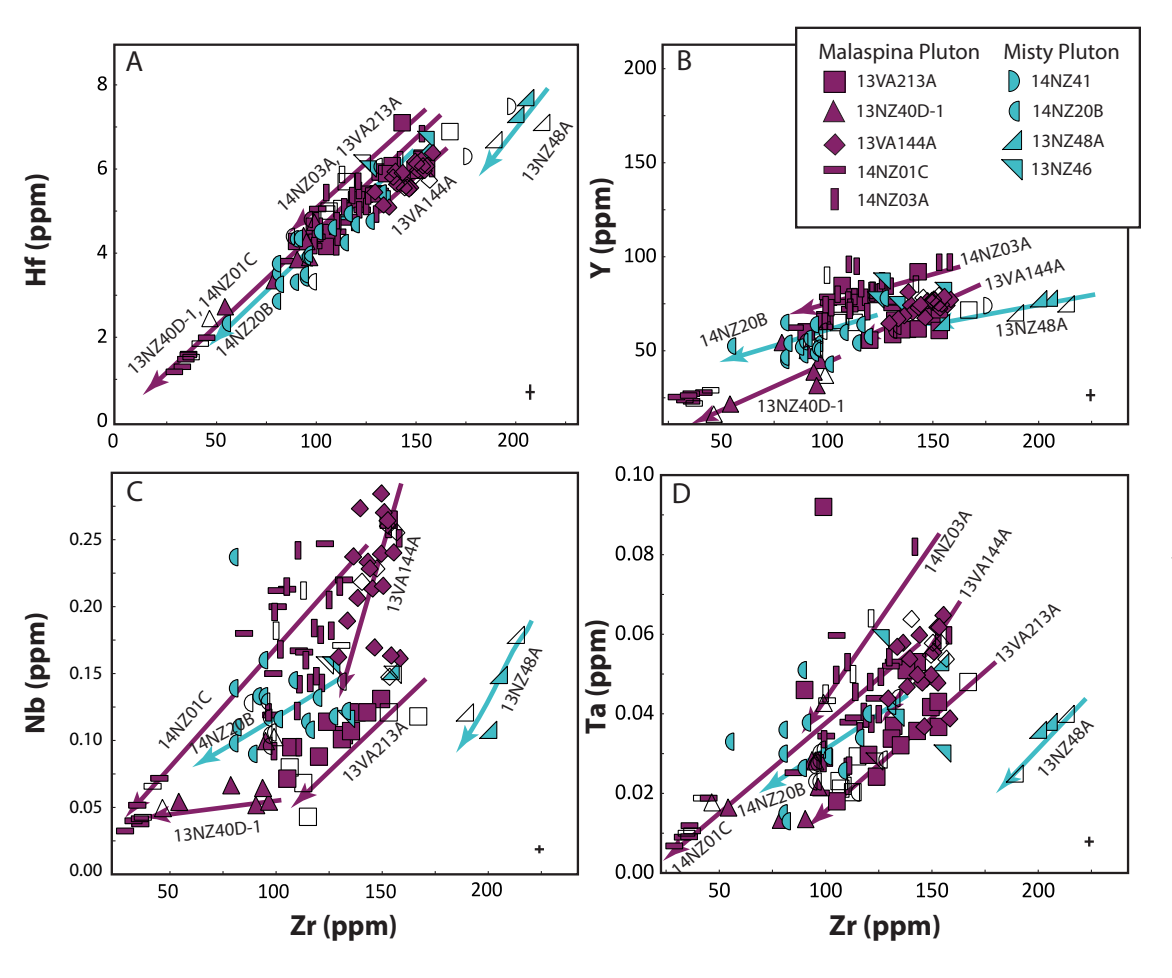


Figure 9. Variation diagrams showing Zr versus selected high-field-strength elements for Misty and Malaspina pluton clinopyroxenes. Colored arrows indicated differentiation trends for each sample. Hollow symbols indicate rim analyses from core-rim traverses. Outliers with unusually high Nb are omitted in panel C. (A) Zr versus Hf. (B) Zr versus Y. (C) Zr versus Nb. (D) Zr versus Ta. The small crosses in each plot indicate typical 10 analytical precision.

 $\pm$  0.14 GPa) and overlap independently calculated Al-in-hornblende pressures determined for samples in the Malaspina and Misty plutons (Carty et al., 2021).

# DISCUSSION

The Median batholith is an archetypal example of a transcrustal cordilleran arc system composed of voluminous, high-Sr/Y plutons (e.g., McCulloch et al., 1987; Muir et al., 1995; Tulloch and Kimbrough, 2003). Tulloch and Kimbrough (2003) first recognized that high-Sr/Y plutons primarily occur in the western (continentward) sector of paired high- and low-Sr/Y Mesozoic magmatic belts in the Median batholith. These high-Sr/Y plutons were emplaced during a surge of Early Cretaceous arc magmatism associated with continentward arc migration

and intra-arc contraction (Daczko et al., 2001; Klepeis et al., 2004, 2007; Marcotte et al., 2005; Scott et al., 2009; Milan et al., 2017; Schwartz et al., 2017, 2021; Carty et al., 2021; Ringwood et al., 2021). They are most abundant in the lower crust (Fiordland segment) where they have been interpreted to reflect deep-crustal partial melting of a mafic, garnet-bearing arc root (McCulloch et al., 1987; Muir et al., 1995; Tulloch and Kimbrough, 2003) or fractionation of igneous garnet (Chapman et al., 2016). A key finding in this study is that igneous clinopyroxenes in the Misty and Malaspina plutons are not in equilibrium with encompassing high-Sr/Y bulk rocks nor with high-Sr/Y melts based on Fe-Mg partitioning relationships and mineral-melt partition coefficients, respectively (Figs. 12 and 13C–13D). In particular, clinopyroxenes are characterized by much lower Sr and Sr/Y values and higher Y than expected for minerals in equilibrium with high-Sr/Y or adaktic melts (Fig. 8). For example, compared to adakites from the Aleutian Islands and from

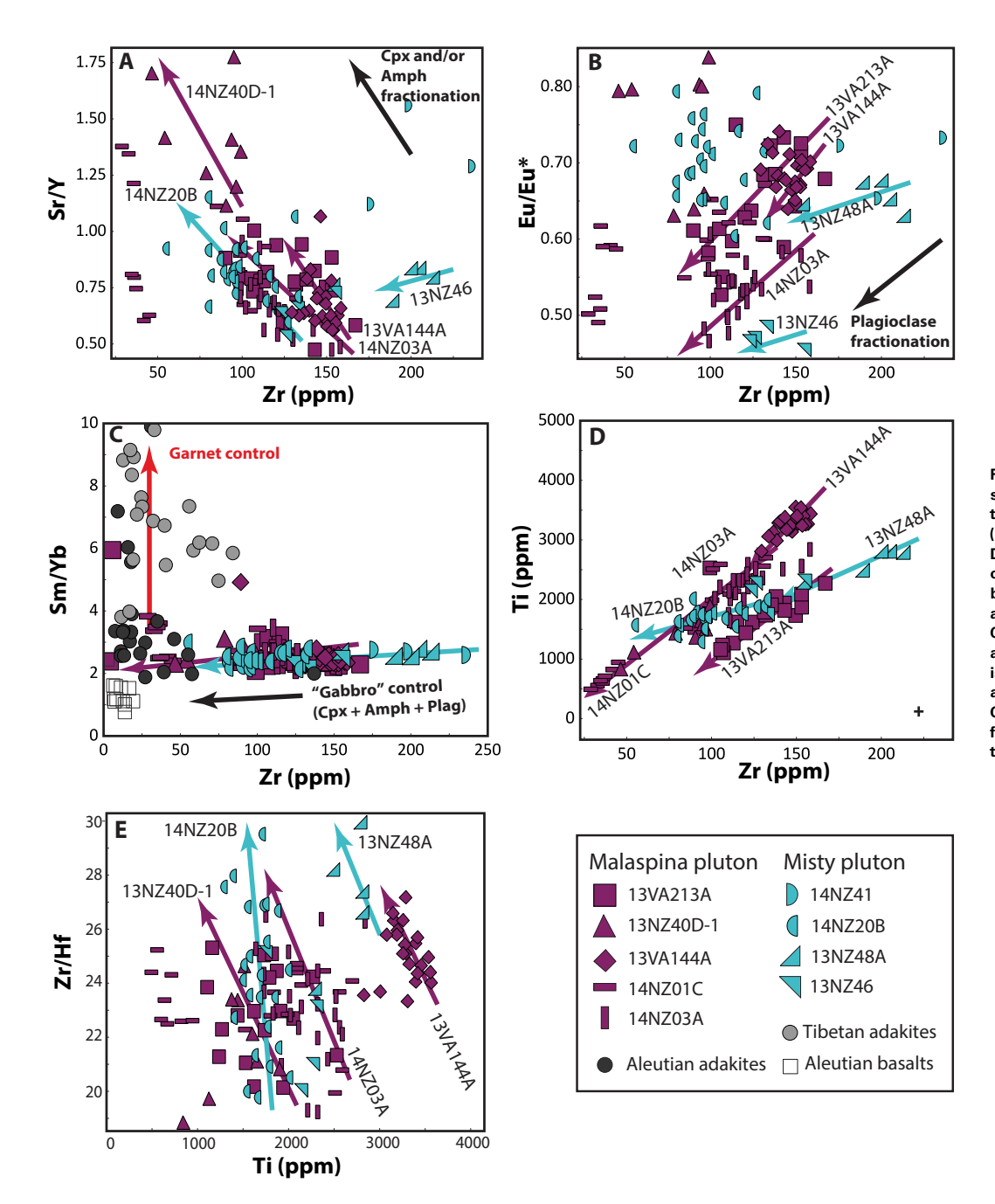
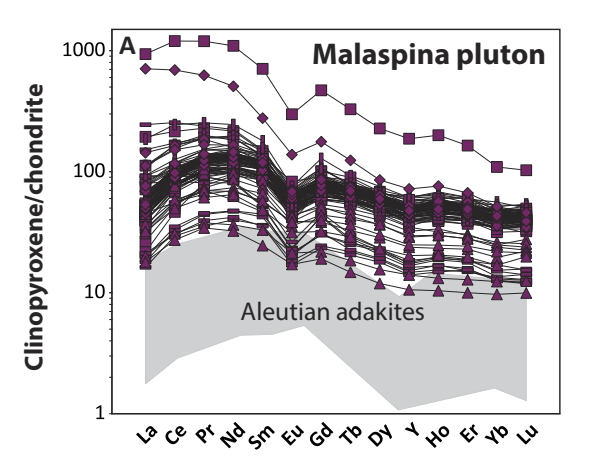


Figure 10. Bivariate diagrams for clinopyroxene samples from the Malaspina and Misty plutons. (A) Zr versus Sr/Y. (B) Zr versus Eu/Eu\*. (C) Zr versus Sm/Yb. Vectors modeled after Davidson et al. (2007) show predicted effects of garnet fractionation (red vector) and "gabbro" (plagioclase [Plag] + clinopyroxene [Cpx] + amphibole [Amph]) fractionation (black vector). Clinopyroxene trace-element data from Aleutian and Tibetian adakites are included for comparison (Yogodzinski and Kelemen, 1998; Zeng et al. 2020). (D) Zr versus Ti. (E) Ti versus Zr/Hf. Colored arrows indicate differentiation trends for each sample. The small cross in D indicates typical 1σ analytical precision.



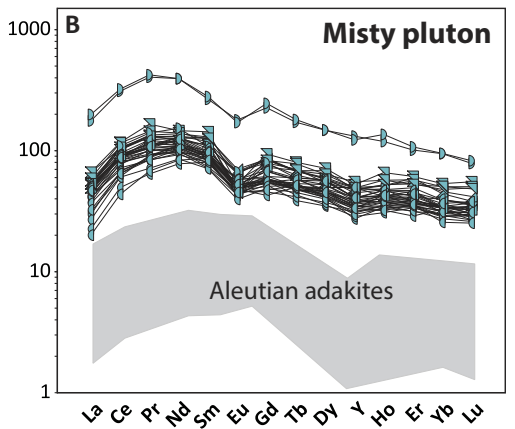


Figure 11. Chondrite-normalized rareearth-element diagrams for clinopyroxene compositions from the Malaspina pluton (A) and Misty pluton (B). Aleutian adakites are shown by gray fields (data from Yogodzinski and Kelemen, 1998). Symbols are the same as in Figure 10.

the Tibetan Plateau (Yogodzinski and Kelemen, 1998; Zeng et al. 2020), igneous clinopyroxenes in the Misty and Malaspina plutons show lower Sr (<100 ppm) and molar Mg# (60–70), which are consistent with derivation from fractionated, low-Sr/Y arc melts (Figs. 8 and 12). Chondrite-normalized REE patterns and Sm/Yb values also show little to no evidence for the significant involvement of garnet (Figs. 10C and 11). Instead, our data are more consistent with "gabbro" (plagioclase + clinopyroxene + amphibole) fractionation (e.g., Davidson et al., 2007).

The low calculated Sr/Y values observed in modeled clinopyroxeneequilibrium melts (<1-26; Fig. 12) are insensitive to the choice of partition coefficient (see Table 5). Thus, the low Sr/Y values of melts in equilibrium with clinopyroxene in this study are intrinsic features of lower-crustal melts in the Median Batholith. Our results are corroborated by independently determined amphibole-equilibrium melt compositions in the Malaspina and Misty plutons, which also give low-Sr/Y melt compositions that diverge from bulk-rock values (Greenberg and Schwartz, 2020; Carty et al., 2021). Collectively, these features suggest that igneous clinopyroxenes in the root of the Median Batholith did not form from crystallization of high-Sr/Y melts. Instead, they are more likely to have been in equilibrium with low-Sr/Y arc magmas formed by partial melting of a hydrous mantle wedge (Fig. 12) (Carty et al., 2021). Thus, we postulate that other processes were likely responsible for the high-Sr/Y bulk-rock chemistry of these rocks, including mineral accumulation (especially plagioclase) and associated melt extraction from the lower crust (e.g., McCarthy and Hasty, 1976; McCarthy and Groves, 1979; Wiebe, 1993; Wiebe et al., 2002; Collins et al., 2006; Deering and Bachmann, 2010; Miller et al., 2011; Vernon and Collins, 2011; Lee and Morton, 2015; Lee et al., 2015; Barnes et al., 2016, 2020; Schaen et al., 2018; Werts et al., 2020; Laurent et al., 2020). Below we examine the conditions at which the clinopyroxenes formed and explore implications for these results with regard to crustal thickness calculations and arc processes in the deep crust of the Median batholith.

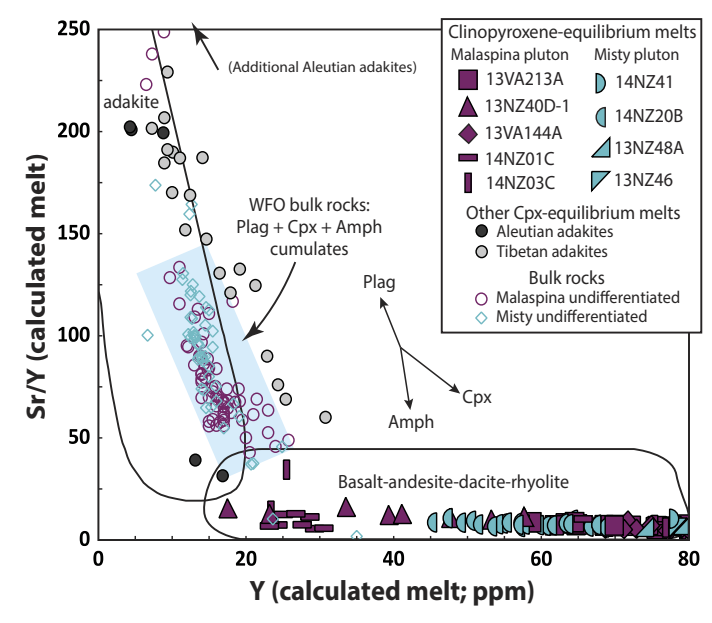


Figure 12. Calculated clinopyroxene-equilibrium melt compositions compared to Western Fiordland Orthogneiss (WFO) bulk-rock data and clinopyroxene-equilibrium melts from other high-Sr/Y rocks. Note that Misty and Malaspina pluton clinopyroxene-equilibrium melt compositions diverge from WFO bulk rocks (blue field) and also from high-Sr/Y clinopyroxenes in adakites from the Aleutian Islands (Alaska, USA) and Tibetan Plateau (gray and black circles; Yogodzinski and Kelemen, 1998; Zeng et al., 2020). Vectors show relative effects of plagioclase (Plag), clinopyroxene (Cpx), and amphibole (Amph) accumulation. The blue field overlapping WFO bulk rocks is interpreted to reflect varying degrees of plagioclase + amphibole + clinopyroxene accumulation.

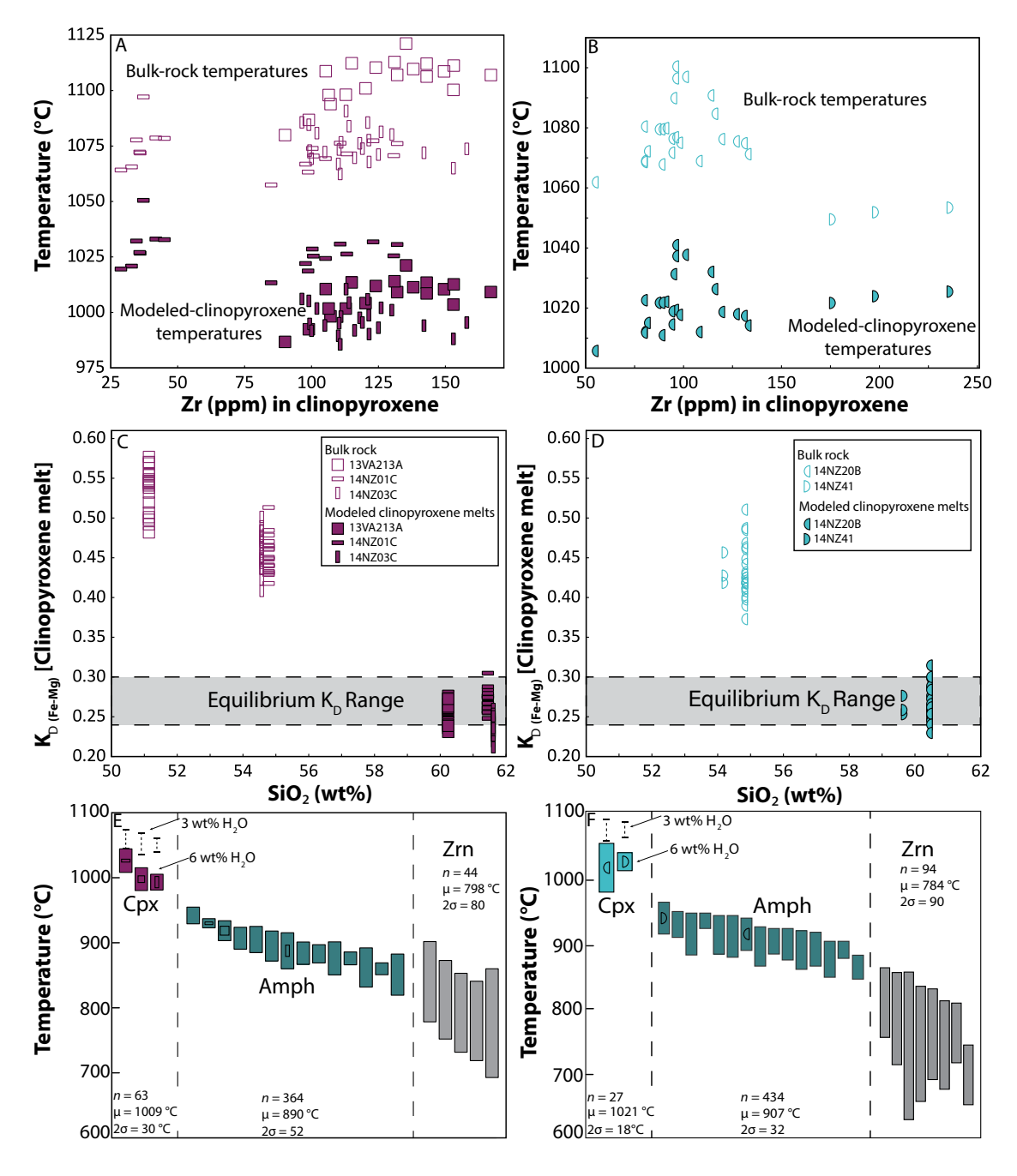


Figure 13. (A-B) Modeled crystallization temperatures for bulk rocks and clinopyroxenes from the Malaspina and Misty pluton thermometry data versus Zr (index of differentiation). Hollow symbols show modeled bulk-rock temperatures, and filled symbols designate calculated clinopyroxene equilibrium melts. The latter show weak decreasing temperature trends with decreasing Zr. (C-D) Comparison of experimental Fe-Mg exchange coefficients (K<sub>D(Fe-Mg)</sub>) for clinopyroxenes assuming melts approximated by bulk rocks (hollow symbols) and amphibole-equilibrium melts (filled symbols). Amphibole-equilibrium melts were calculated from coexisting hornblendes in the same samples. (E-F) Modeled crystallization temperatures for igneous clinopyroxene (Cpx), hornblende (amphibole, Amph), and zircon (Zrn) in the Malaspina and Misty plutons. Amphibole data are from Carty et al. (2021) and Greenberg and Schwartz (2020); zircon data are from Schwartz et al. (2017). Colored bars show calculated crystallization temperatures at 6 wt% H<sub>2</sub>O for clinopyroxenes centered around the mean for each sample and extending to ±2σ. Dashed bars show temperatures at 3 wt% H<sub>2</sub>O; µ indicates mean value. Modeled clinopyroxene temperatures are calculated according to Neave and Putirka (2017).

# **Conditions of Magma Emplacement**

In order to assess P-T conditions of crystallization, we calculated model clinopyroxene temperatures following Putirka (2008), which requires an assumption about melt compositions in equilibrium with clinopyroxene. We calculated model temperatures in two ways, by assuming: (1) melt compositions are approximated by encompassing bulk-rock compositions, and (2) melts were similar to amphibole-equilibrium melt compositions derived from coexisting hornblendes and the chemometric equations of Zhang et al. (2017). In the case of bulk-rock melt compositions, calculated clinopyroxene crystallization temperatures range from 1050 °C to 1121 °C assuming 6 wt% H<sub>2</sub>O and 1090 °C to 1167 °C assuming 3 wt% H<sub>2</sub>O. Alternatively, assuming clinopyroxenes were in equilibrium with modeled melts based on amphibole compositions, calculations yield lower clinopyroxene crystallization temperatures ranging from 986 °C to 1051 °C assuming 6 wt%  $H_2O$  and 1035 °C to 1087 °C assuming 3 wt% H<sub>2</sub>O (Figs. 13A-13B). In general, the bulk-rock values give temperatures that are ~50-75 °C higher than calculated amphibole-equilibrium melts and they also do not overlap amphibole crystallization temperatures despite petrographic evidence for coexistence with igneous amphibole in most samples in this study (Figs. 13E-13F).

To evaluate equilibrium between clinopyroxenes and assumed melts and the validity of resulting temperatures, we compared Fe-Mg exchange coefficients (K<sub>D(Fe-Mol</sub>) in the cases of both bulk-rock and amphibole-equilibrium melt compositions. Figures 13C-13D show the experimentally predicted range of K<sub>D(Fe-Mo)</sub> values (horizontal gray bar at 0.27  $\pm$  0.03) and calculated  $K_{D(Fe-Mg)}$  values for both cases. For the bulk-rock melts, K<sub>D</sub> values (0.37–0.58) deviate significantly from the experimentally predicted range, whereas those assuming amphibole-equilibrium melts (0.21-0.31) overlap the predicted range(Figs. 13C-13D). These results demonstrate that melts approximated by bulk-rock compositions are not in equilibrium with clinopyroxenes, and therefore resulting temperatures are not geologically meaningful. Although we cannot prove that the modeled melts were the exact compositions from which the clinopyroxenes crystallized, the equilibrium melt compositions are geologically reasonable in terms of their calculated K<sub>D(Fe-Mg)</sub> values and thus we consider them to be likely close estimates (see uncertainty estimates in Results). Therefore, we view temperatures of 986-1051 °C at 6 wt% H<sub>2</sub>O or 1035-1087 °C at 3 wt% H<sub>2</sub>O as the best approximations for clinopyroxene crystallization in the lower crust.

Figures 13E-13F show a compilation of igneous temperature data from the Malaspina and Misty plutons integrating modeled clinopyroxene, amphibole, and Ti-in-zircon temperatures (Schwartz et al., 2017; Carty et al., 2021; this study). In both plutons, the data show a consistent pattern of initial emplacement at ~1050 °C and cooling of ~250-300 °C to ~750 °C (Figs. 13E-13F). Some variation in P-T conditions is suggested by differences in clinopyroxene major-element chemistry (Figs. 7A-7B), and a broader data set of clinopyroxene thermometry would likely show more variations in initial temperatures. These results are consistent with petrographic observations of relict igneous assemblages that show clinopyroxene as an early-crystallizing phase followed by plagioclase and amphibole (Fig. 5). These observations are mirrored in the thermometry data, whereby clinopyroxene crystallization temperatures are consistently hotter compared to amphibole temperatures but also overlap. Clinopyroxenes and amphiboles also show negative Eu anomalies that are consistent with co-precipitation of plagioclase. Zircons give much lower temperatures compared to clinopyroxenes, and we do not observe any correlation between Zr/Hf and either Ti or Zr (indexes of fractionation) in our clinopyroxene geochemical data (Figs. 10D-10E). Because zircon is one of the few minerals that would significantly fractionate Zr/Hf, our data are thus consistent with clinopyroxene crystallization in the absence of zircon, as also indicated by the crystallization temperature ranges shown in Figures 13E–13F.

In high-pressure crystallization experiments of andesitic melts, igneous garnet is initially saturated at 1.0-1.2 GPa (Alonso-Perez et al., 2009; Ulmer et al., 2018), and the absence of garnet signatures in chondrite-normalized heavy REE patterns (Figs. 9 and 10C) suggests that garnet was not present as a fractionating or residual phase in the Malaspina and Misty plutons. Modeled clinopyroxene crystallization pressures range from 0.95 to 1.14 GPa depending on assumed water content, and these values are at or below pressures at which igneous garnet is expected to become stable. Similar pressures are observed in contact-aureole estimates, which have large uncertainties (1.0-1.5 GPa; Allibone et al., 2009b), and Al-in-hornblende results from the Malaspina pluton (0.92 ± 0.09 GPa; Carty et al., 2021). The absence of garnet as an igneous phase in our samples and the lack of geochemical evidence for garnet in the petrogenesis of the clinopyroxenes suggest that emplacement pressures were slightly below the ~1.0 GPa garnet stability pressure (Alonso-Perez et al., 2009; Ulmer et al., 2018). Thus, we conclude that the high-Sr/Y signatures in bulk-rock data are not attributable to fractionation of igneous garnet.

# **Implications for Moho Depth Correlations**

To examine implications for the use of bulk-rock Sr/Y values as a proxy for crustal thickness (e.g., Chapman et al., 2015; Mantle and Collins, 2008; Profeta et al., 2015; Zeng et al., 2020), we examined 104 bulk-rock analyses from the Malaspina and Misty plutons and calculated Moho depths based on the Chapman et al. (2015) calibration (see the Supplemental Material). We applied filters established by Chapman et al. (2015) (MgO = 1-6 wt%; SiO<sub>2</sub> = 55-70 wt%), which resulted in the exclusion of almost all samples analyzed in this study. Only 5.8% of analyses in the broader dataset (6/104) are within the calibration, and they yield an average Moho depth of 69 km ( $\sigma$  = 8 km). This value is much greater than estimates for Malaspina pluton emplacement (Allibone et al., 2009a; Carty et al., 2021; this study) and would imply that melts had traversed >30 km of crust prior to emplacement.

Mantle and Collins (2008) proposed another depth proxy for mafic rocks based on the empirical correlation between bulk-rock Ce/Y values and crustal thickness. We filtered the same 104 bulk-rock analyses for the Malaspina and Misty plutons using the same parameters as Mantle and Collins (2008) (MgO >4 wt%;  $SiO_2 = 44-53$  wt%), which resulted in the exclusion of >80% of analyses in the broader dataset. The maximum calculated Moho depth using the Mantle and Collins (2008) Ce/Y proxy for the remaining 20 bulk-rock analyses is  $47 \pm 3$  km for the Malaspina pluton and  $38 \pm 3$  km for the Misty pluton. These values are consistent with independently determined emplacement depths and metamorphic pressures shortly after igneous emplacement (Allibone et al., 2009; DePaoli et al., 2009; Stowell et al., 2014).

Taken together, the exclusion of most samples with >55 wt%  ${\rm SiO_2}$  from the Sr/Y–Moho depth calibration along with the unrealistic predicted crustal thickness suggests that Malaspina pluton and Misty pluton bulk rocks do not likely have liquid compositions and are more consistent with being cumulates (see below). Our results do not invalidate the Sr/Y depth proxy in other systems, particularly those where Ce/Y and Sr/Y depth results agree; however, our results emphasize the importance of using multiple proxies in evaluating paleo–crustal thickness in arcs. We also note that while the Ce/Y Moho proxy does give results more consistent with metamorphic pressures, it is uncertain whether this is a fortuitous result or whether the Ce/Y proxy is less sensitive to plagioclase accumulation effects because Ce is at least an order of magnitude less compatible in plagioclase than Sr (e.g., Severs et al., 2009), and the Mantle and Collins (2008) proxy filters plagioclase cumulates.

# Implications for High-Sr/Y Signatures in Lower-Arc Crust

The prominent and widely cited high-Sr/Y signature in bulk-rock studies of the Malaspina and Misty plutons is clearly absent in our modeled melts in equilibrium with analyzed clinopyroxenes, which instead closely resemble typical arc magmas (Fig. 12). If bulk-rock compositions are not equivalent to parent magma compositions, this raises the question: What is the significance of high bulk-rock Sr/Y signatures in cordilleran plutons?

In the case of the Malaspina and Misty plutons, various lines of reasoning indicate that their high-Sr/Y signatures predominantly reflect plagioclase accumulation (see Fig. 1D). For example, Stevenson et al. (2005) and Tulloch and Palin (2013) used laser-ablation mass spectrometry to demonstrate that plagioclase feldspars in the Western Fiordland Orthogneiss are characterized by very high Sr concentrations (>1000 ppm) compared to low-Sr/Y Mesozoic arc rocks in Fiordland. Accumulation of even modest amounts of Sr-rich plagioclase would therefore dominate the bulk-rock Sr budget and would drive bulk-rock compositions toward higher Sr/Y values relative to original melt compositions. This effect is illustrated in Figure 12, where bulk-rock data are plotted against calculated clinopyroxene-equilibrium melt compositions. Bulk rocks plot along an array that is consistent with variable plagioclase accumulation (see the blue field and vectors in Fig. 12), in contrast to clinopyroxene-equilibrium melts, which plot in the typical arc basalt-andesite-dacite-rhyolite field.

Accumulation of minerals that preferentially sequester Y would have the opposite net effect compared to plagioclase and would drive Sr/Y down in bulk-rock samples. Zircon accumulation is one possibility; however, zircon is

a trace mineral in these rocks (<1 wt%) and concentrations of Y are modest (100–1000 ppm; Schwartz et al., 2017). Bulk-rock zirconium concentrations are also below those required for zircon saturation at temperatures indicated by Ti-in-zircon thermometry (Watson and Harrison, 1983); thus, bulk rocks cannot be zircon cumulates, and zircon accumulation is unlikely to have a significant effect on the Sr/Y values in these rocks. Clinopyroxene and amphibole accumulation would also decrease the Sr/Y ratio (see representative mineral vectors in Fig. 12). Accumulation of Mg-rich minerals like clinopyroxene and amphibole can also explain the disequilibrium  $K_{\text{D(Fe-Mg)}}$  values between bulk rocks and clinopyroxenes (Figs. 13C–13D). Collectively, these observations are consistent with Misty and Malaspina pluton bulk rocks being cumulates of plagioclase + clinopyroxene  $\pm$  amphibole (see preferred model in Fig. 1D).

The interpretation of most Misty and Malaspina pluton bulk rocks as cumulates has broad implications for understanding the development of the Median batholith and magmatic processes in the lower crust of cordilleran arcs. For the Median batholith, the cumulate nature of the high-Sr/Y plutons requires reevaluation of magma sources in the Mesozoic Median batholith as well as the role of garnet in the petrogenesis of Separation Point Suite granites and the Western Fiordland Orthogneiss. While the distinction between plutons in the inboard (Separation Point Suite) and outboard (Darran Suite) belts is based on bulk-rock chemistry (Tulloch and Kimbrough, 2003), it remains unclear whether melt compositions in the two belts reflect distinct melt sources or whether differences instead reflect varying crystal-accumulation and melt-segregation processes from similar parental magmas. In support of the latter, Tulloch and Kimbrough (2003) reported similarities in major-element compositions and differentiation trends (e.g., modified alkali lime index) between the Separation Point and Darran Suites, and Schwartz et al. (2021) showed that stable and radiogenic isotopes in zircons are also nearly identical for rocks in the same geographic region. In addition, the distinction between high- and low-Sr/Y suites is not always straightforward; some Western Fiordland Orthogneiss bulk rocks have low Sr/Y ratios (Fig. 4D), and some Darran Suite bulk rocks have high Sr/Y values (e.g., Turnbull et al., 2010). In the case of the latter, Turnbull et al. (2010) also concluded that high-Sr/Y signatures in the Halfmoon pluton (Darran Suite) were generated by plagioclase accumulation, as we propose here for the Western Fiordland Orthogneiss. Therefore, we speculate that differences in bulk-rock trace elements (e.g., Sr, Y) primarily reflect varying degrees of crystal accumulation and not major differences in parental magma chemistry nor significant involvement of garnet (contrast models in Fig. 1C and Fig. 1D) (e.g., McCulloch et al., 1987; Tulloch and Kimbrough, 2003; Chapman et al., 2017).

An implication of our cumulate interpretation is that bulk-rock values in the Western Fiordland Orthogneiss may not be particularly meaningful in terms of original melt compositions, and this has bearing on the use of bulk rocks for geochemical melt modeling in the lower crust of arcs. Similar conclusions regarding the cumulate nature of other arc-related plutonic rocks have been reached by other researchers (e.g., Barnes et al., 2020), and we suggest that this shift away from the use bulk-rock melt proxies is inevitable as analytical techniques continue to evolve, revealing the complexity of these

subduction-related magma systems. For example, previous work based on geochemical modeling of bulk rocks in the Western Fiordland Orthogneiss predicted the production of a thick, garnet-bearing arc root (McCulloch et al., 1987; Muir et al., 1995; Chapman et al., 2017). Instead, our data suggest that variations in bulk-rock values are the result of crystal accumulation and melt loss, not fractionation of igneous garnet. Thus, our data do not support the production of a voluminous garnet-bearing residue, and this result implies that the major flareup-related plutons did not necessarily generate a thick, gravitationally unstable arclogite root. Consequently, foundering of the arc root may have been a minor mechanism in the subsequent orogenic collapse of the arc starting at ca. 108-106 Ma and continuing to ca. 90 Ma (Tulloch et al., 2009; Klepeis et al., 2016; Schwartz et al., 2016; Chapman et al., 2017). Moreover, the use of high-Sr/Y plutons as an indicator of Early Cretaceous crustal thickening in the Median batholith may also require reevaluation.

The large size of the plagioclase-rich cumulate residue in the lower crust of Fiordland (>2300 km²) also implies highly efficient crystal-accumulation and melt-extraction processes to shallower crustal levels. One possibility is that these processes were aided by unusually high magma addition rates during the Early Cretaceous arc flareup (Milan et al., 2017; Schwartz et al., 2017; Ringwood et al., 2021). Resultant high heat flow and melt input into the lower crust would have allowed for extensive magma bodies to form (Werts et al., 2020), thereby generating voluminous, high-Sr/Y arc cumulates. Similar high-Sr/Y rocks also occur in association with arc flareups in Jurassic and Cretaceous rocks of the Sierra Nevada batholith (California; Cecil et al., 2012), and we speculate that high-magma-addition-rate events may be associated with the production of high-Sr/Y cumulates in the roots of other cordilleran arcs. High magma addition rates and high heat flow would also have allowed for extensive melt differentiation in the lower crust and the production of derivative intermediate to silicic melts via crystal fractionation. The ascent of these silicic melts from the lower to the middle crust may have been driven by a combination of "mush-zone" processes, including crystal settling and compaction, gas filter pressing, and/or melt migration along crystal-plastic shear zones like those that traverse the lower and middle crust of Fiordland (see yellow shear zones in Fig. 2) (Klepeis et al., 2004, 2007). Extraction and redistribution of these melts is likely responsible for the emplacement of coeval high-Sr/Y plutons in the upper and middle crust (e.g., Allibone et al., 2009c). The preservation of these rocks in Fiordland as well as shear zones that link the lower and middle crust presents a future opportunity for further investigating crystal-liquid segregation and melt redistribution processes during continental crust construction in a well-preserved transcrustal magmatic arc system.

# CONCLUSIONS

Geochemical analysis of igneous clinopyroxenes in the Misty and Malaspina plutons lead to the following conclusions about the formation of high-Sr/Y plutonic rocks in the lower crust of the Median batholith:

- (1) Significant discrepancies exist between bulk-rock geochemistry and modeled melt compositions from relict igneous pyroxenes, and bulk-rock high-Sr/Y signatures cannot be reproduced using appropriate mineral-melt partition coefficients.
- (2) Fe-Mg exchange coefficients for bulk rocks deviate from the experimentally predicted range and yield unrealistic results. This observation suggests that bulk rocks are not in equilibrium with clinopyroxenes. In contrast, Fe-Mg exchange coefficients for modeled amphiboleequilibrium melts overlap the experimentally predicted range, indicating that they are acceptable (though nonunique) proxies for melts in equilibrium with clinopyroxenes.
- (3) Model clinopyroxene temperatures using amphibole-equilibrium melt compositions (1050-1121 °C at 6 wt% H<sub>2</sub>O) are slightly higher than amphibole crystallization temperatures (Carty et al., 2021) and are consistent with petrographic observations for early clinopyroxene crystallization before amphibole. Modeled clinopyroxene pressures give emplacement values of ≤1.0 GPa, similar to Al-in-hornblende results from the Malaspina pluton.
- (4) Most bulk-rock samples from the Malaspina and Misty plutons lie outside the calibration of the Chapman et al. (2015) Sr/Y-Moho depth relationship. Those values that do lie within the calibration yield Moho depths (average = 69 km) much greater than predicted from contact-aureole studies, Al-in-hornblende barometry, and our modeled clinopyroxene pressures. Calculated crustal thickness estimates based on Ce/Y ratios from the Mantle and Collins (2008) relationship give more reasonable results (39-47 km).
- (5) Our data indicate that high-Sr/Y signatures in the Malaspina and Misty plutons reflect accumulation of Sr-rich plagioclase rather than involvement of garnet as a residual or fractionating phase.
- (6) Bulk-rock compositions are therefore poor proxies for melt compositions in the Western Fiordland Orthogneiss. Consequently, bulk-rock values are inappropriate for melt evolution modeling and would erroneously predict a thick, garnet-bearing arc root.
- (7) The inboard belt of the Mesozoic Median batholith primarily represents a lower-crustal cumulate zone formed from combined accumulation of plagioclase (+ clinopyroxene + amphibole) and loss of interstitial liquid. We speculate that melt extraction was aided by unusually high magma addition rates during the Early Cretaceous arc flareup, resulting in efficient crystal-liquid segregation and the redistribution of melts from an extensive lower-crustal, crystal-rich mush zone to mid-crustal storage regions.

#### ACKNOWLEDGMENTS

We thank Mandy and Richard Abernethy (Fiordland Expeditions) and Seán Ellis and Maria Kuster (Pure Salt) for assistance with sampling. The New Zealand Department of Conservation, Te Anau office, is also thanked for allowing access and sampling in Fiordland, Jade Star Lackey and Jonathan Harris are thanked for assistance with XRF analyses. Zhan Peng, Talen Wickenden, and

Gillian Greenberg are thanked for LA-ICPMS assistance. We appreciate conversations with and earlier reviews of this manuscript by Elena Miranda, Keith Klepeis, Rose Turnbull, Andy Tulloch, and Harold Stowell. Helpful suggestions by two anonymous reviewers, Science Editor Shan De Silva, and Associate Editor Alan Whittington greatly improved this manuscript. Financial support for this project was provided by the U.S. National Science Foundation grants EAR-40015228 to Schwartz and EAR-1655152 to R. Cecil and Schwartz.

#### REFERENCES CITED

- Allibone, A.H., Jongens, R., Turnbull, I.M., Milan, L.A., Daczko, N.R., DePaoli, M.C., and Tulloch, A.J., 2009a, Plutonic rocks of Western Fiordland, New Zealand: Field relations, geochemistry, correlation, and nomenclature: New Zealand Journal of Geology and Geophysics, v. 52, p. 379–415, https://doi.org/10.1080/00288306.2009.9518465.
- Allibone, A.H., Milan, L.A., Daczko, N.R., and Turnbull, I.M., 2009b, Granulite facies thermal aureoles and metastable amphibolite facies assemblages adjacent to the Western Fiordland Orthogneiss in southwest Fiordland, New Zealand: Journal of Metamorphic Geology, v. 27, p. 349–369, https://doi.org/10.1111/j.1525-1314.2009.00822.x.
- Allibone, A.H., Jongens, R., Scott, J.M., Tulloch, A.J., Turnbull, I.M., Cooper, A.F., Powell, N.G., Ladley, E.B., King, R.P., and Rattenbury, M.S., 2009c, Plutonic rocks of the Median Batholith in eastern and central Fiordland, New Zealand: Field relations, geochemistry, correlation, and nomenclature: New Zealand Journal of Geology and Geophysics, v. 52, p. 101–148, https://doi.org/10.1080/00288300909509882.
- Alonso-Perez, R., Müntener, O., and Ulmer, P., 2009, Igneous garnet and amphibole fractionation in the roots of island arcs: Experimental constraints on andesitic liquids: Contributions to Mineralogy and Petrology, v. 157, p. 541–558, https://doi.org/10.1007/s00410-008-0351-8.
- Ardill, K., Paterson, S., and Memeti, V., 2018, Spatiotemporal magmatic focusing in upper-mid crustal plutons of the Sierra Nevada arc: Earth and Planetary Science Letters, v. 498, p. 88–100, https://doi.org/10.1016/j.epsl.2018.06.023.
- Barnes, C.G., Count, N., and Yoshinobu, A., 2016, Crystal accumulation in a tilted arc batholith: American Mineralogist, v. 101, p. 1719–1734, https://doi.org/10.2138/am-2016-5404.
- Barnes, C.G., Werts, K., Memeti, V., and Ardill, K., 2020, Most granitoid rocks are cumulates: Deductions from hornblende compositions and zircon saturation: Journal of Petrology, v. 60, p. 2227–2240, https://doi.org/10.1093/petrology/egaa008.
- Blundy, J.D., Robinson, J.A.C., and Wood, B.J., 1998, Heavy REE are compatible in clinopyroxene on the spinel lherzolite solidus: Earth and Planetary Science Letters, v. 160, p. 493–504, https://doi.org/10.1016/S0012-821X(98)00106-X.
- Bolhar, R., Weaver, S.D., Whitehouse, M.J., Palin, J.M., Woodhead, J.D., and Cole, J.W., 2008, Sources and evolution of arc magmas inferred from coupled O and Hf isotope systematics of plutonic zircons from the Cretaceous Separation Point Suite (New Zealand): Earth and Planetary Science Letters, v. 268, p. 312–324, https://doi.org/10.1016/j.epsl.2008.01.022.
- Carty, K., Schwartz, J.J., Wiesenfeld, J., Klepeis, K.A., Stowell, H.H., Tulloch, A.J., and Barnes, C.G., 2021, The generation of arc andesites and dacites in the lower crust of a cordilleran arc, Fiordland, New Zealand: Journal of Petrology, v. 62, no. 9., egab043, https://doi.org/10.1093/petrology/egab043.
- Cecil, M.R., Rotberg, G.L., Ducea, M.N., Saleeby, J.B., and Gehrels, G.E., 2012, Magmatic growth and batholithic root development in the northern Sierra Nevada, California: Geosphere, v. 8, p. 592–606, https://doi.org/10.1130/GES00729.1.
- Chantler, C.T., Olsen, K., Dragoset, R.A., Chang, J., Kishore, A.R., Kotochigova, S.A., and Zucker, D.S., 2005, X-ray form factor, attenuation and scattering tables (version 2.1): U.S. National Institute of Standards and Technology Standard Reference Database 66, https://doi.org/10.18434/T4HS32.
- Chapman, J.B., Ducea, M.N., DeCelles, P.G., and Profeta, L., 2015, Tracking changes in crustal thickness during orogenic evolution with Sr/Y: An example from the North American Cordillera: Geology, v. 43, p. 919–922, https://doi.org/10.1130/G36996.1.
- Chapman. T., Clarke, G.L., and Daczko, N.R., 2016, Crustal differentiation in a thickened arc—Evaluating depth dependences: Journal of Petrology, v. 57, p. 595–620, https://doi.org/10.1093/petrology/egw022.
- Chapman, T., Clarke, G.L., Piazolo, S., and Daczko, N.R., 2017, Evaluating the importance of metamorphism in the foundering of continental crust: Scientific Reports, v. 7, 13039, https://doi .org/10.1038/s41598-017-13221-6.

- Chiaradia, M., 2015, Crustal thickness control on Sr/Y signatures of recent arc magmas: An Earth scale perspective: Scientific Reports, v. 5, 8115, https://doi.org/10.1038/srep08115.
- Clarke, G.L., Daczko, N.R., and Miescher, D., 2013, Identifying relic igneous garnet and clinopy-roxene in eclogite and granulite, Breaksea Orthogneiss, New Zealand: Journal of Petrology, v. 54, p. 1921–1938, https://doi.org/10.1093/petrology/eqt036.
- Collins, W.J., Wiebe, R.A., Healy, B., and Richards, S.W., 2006, Replenishment, crystal accumulation and floor aggradation in the megacrystic Kameruka Suite, Australia: Journal of Petrology, v. 47, p. 2073–2104, https://doi.org/10.1093/petrology/egl037.
- Coombs, D.S., Landis, C.A., Norris, R.J., Sinton, J.M., Borns, D.J., and Craw, D., 1976, The Dun Mountain ophiolite belt, New Zealand, its tectonic setting, constitution and origin, with special reference to the southern portion: American Journal of Science, v. 276, p. 561–603.
- Daczko, N.R., Klepeis, K.A., and Clarke, G.L., 2001, Evidence of Early Cretaceous collisional-style orogenesis in northern Fiordland, New Zealand and its effects on the evolution of the lower crust: Journal of Structural Geology, v. 23, p. 693–713, https://doi.org/10.1016/S0191-8141 (00)00130-9
- Davidson, J., Turner, S., Handley, H., Macpherson, C., and Dosseto, A., 2007, Amphibole "sponge" in arc crust?: Geology, v. 35, p. 787–790, https://doi.org/10.1130/G23637A.1.
- Decker, M., Schwartz, J.J., Stowell, H.H., Klepeis, K.A., Tulloch, A.J., Kitajima, K., Valley, J.W., and Kylander-Clark, A.R.C., 2017, Slab-triggered arc flare-up in the Cretaceous Median Batholith and the growth of lower arc crust, Fiordland, New Zealand: Journal of Petrology, v. 58, p. 1145–1171, https://doi.org/10.1093/petrology/egx049.
- Deering, C.D., and Bachmann, O., 2010, Trace element indicators of crystal accumulation in silicic igneous rocks: Earth and Planetary Science Letters, v. 297, p. 324–331, https://doi.org/10.1016/j.epsl.2010.06.034.
- Defant, M.J., and Drummond, M.S., 1990, Derivation of some modern arc magmas by melting of young subducted lithosphere: Nature, v. 347, p. 662–665, https://doi.org/10.1038/347662a0.
- De Paoli, M.C., Clarke, G.L., Klepeis, K.A., Allibone, A.H., and Turnbull, I.M., 2009, The eclogite-granulite transition: Mafic and intermediate assemblages at Breaksea Sound, New Zealand: Journal of Petrology, v. 50, p. 2307–2343, https://doi.org/10.1093/petrology/egp078.
- Ducea, M.N., Chapman, A.D., Bowman, E., and Tryantafyllou, A., 2020a, Arclogites and their role in continental evolution; Part 1: Background, locations, petrography, geochemistry, chronology and thermobarometry: Earth-Science Reviews, v. 214, 103375, https://doi.org/10.1016/j .earscirev.2020.103375.
- Ducea, M.N., Chapman, A.D., Bowman, E., and Balica, C., 2020b, Arclogites and their role in continental evolution; Part 2: Relationship to batholiths and volcanoes, density and foundering, remelting and long-term storage in the mantle: Earth-Science Reviews, v. 214, 103476, https://doi.org/10.1016/j.earscirev.2020.103476.
- Ewart, A., and Griffin, W.L., 1994, Application of proton-microprobe data to trace-element partitioning in volcanic rocks: Chemical Geology, v. 117, p. 251–284, https://doi.org/10.1016/0009-2541(94)90131-7.
- Flowers, R.M., Bowring, S.A., Tulloch, A.J., and Klepeis, K.A., 2005, Tempo of burial and exhumation within the deep roots of a magmatic arc, Fiordland, New Zealand: Geology, v. 33, p. 17–20, https://doi.org/10.1130/G21010.1.
- Green, T.H., Blundy, J.D., Adam, J., and Yaxley, G.M., 2000, SIMS determination of trace element partition coefficients between garnet, clinopyroxene and hydrous basaltic liquids at 2–7.5 GPa and 1080–1200°C: Lithos, v. 53, p. 165–187, https://doi.org/10.1016/S0024-4937(00)00023-2.
- Greenberg, G., and Schwartz, J., 2020, Tracking the geochemical evolution of arc melts from lower-crustal MASH zone to mid-crustal melt reservoir, Fiordland, New Zealand: Abstract presented at Goldschmidt2020 Conference, virtual, 21–26 June, https://doi.org/10.46427/gold2020.876.
- Hawkesworth, C.J., and Kemp, A.I.S., 2006, Using hafnium and oxygen isotopes in zircons to unravel the record of crustal evolution: Chemical Geology, v. 226, p. 144–162, https://doi.org/10.1016/j.chemgeo.2005.09.018.
- Karlstrom, L., Lee, C.-T.A., and Manga, M., 2014, The role of magmatically driven lithospheric thickening on arc front migration: Geochemistry Geophysics Geosystems, v. 15, p. 2655–2675, https://doi.org/10.1002/2014GC005355.
- Kelemen, P.B., 1995, Genesis of high Mg# andesites and the continental crust: Contributions to Mineralogy and Petrology, v. 120, p. 1–19, https://doi.org/10.1007/BF00311004.
- Kelemen, P.B., Hanghøj, K., and Greene, A.R., 2014, One view of the geochemistry of subduction-related magmatic arcs, with an emphasis on primitive andesite and lower crust, in Rudnick, R.L., ed., Treatise on Geochemistry (second edition), Volume 4: The Crust: Amsterdam, Elsevier, p. 749–806, https://doi.org/10.1016/B978-0-08-095975-7.00323-5.

- Kirsch, M., Paterson, S.R., Wobbe, F., Ardila, A.M.M., Clausen, B.L., and Alasino, P.H., 2016, Temporal histories of Cordilleran continental arcs: Testing models for magmatic episodicity: American Mineralogist, v. 101, p. 2133–2154, https://doi.org/10.2138/am-2016-5718.
- Klepeis, K.A., Clarke, G.L., Gehrels, G., and Vervoort, J., 2004, Processes controlling vertical coupling and decoupling between the upper and lower crust of orogens: Results from Fiordland, New Zealand: Journal of Structural Geology, v. 26, p. 765–791, https://doi.org/10.1016 /i.isa.2003.08.012.
- Klepeis, K.A., King, D., De Paoli, M., Clarke, G.L., and Gehrels, G., 2007, Interaction of strong lower and weak middle crust during lithospheric extension in western New Zealand: Tectonics, v. 26, TC4017, https://doi.org/10.1029/2006TC002003.
- Klepeis, K.A., Schwartz, J.J., Stowell, H.H., and Tulloch, A.J., 2016, Gneiss domes, vertical and horizontal mass transfer, and the initiation of extension in the hot lower-crustal root of a continental arc, Fiordland, New Zealand: Lithosphere, v. 8, p. 116–140, https://doi.org/10.1130/L490.1.
- Klepeis, K., Webb, L., Blatchford, H., Schwartz, J., Jongens, R., Turnbull, R., and Stowell, H., 2019, Deep slab collision during Miocene subduction causes uplift along crustal-scale reverse faults in Fiordland, New Zealand: GSA Today, v. 29, no. 9, p. 4–10, https://doi.org/10.1130/GSATG399A.1.
- Lackey, J.S., Cecil, M.R., Windham, C.J., Frazer, R.E., Bindeman, I.N., and Gehrels, G.E., 2012, The Fine Gold Intrusive Suite: The roles of basement terranes and magma source development in the Early Cretaceous Sierra Nevada batholith: Geosphere, v. 8, p. 292–313, https://doi.org /10.1130/GES00745.1.
- Laurent, O., Björnsen, J., Wotzlaw, J.-F., Bretscher, S., Silva, M.P., Moyen, J.-F., Ulmer, P., and Bachmann, O., 2020, Earth's earliest granitoids are crystal-rich magma reservoirs tapped by silicic eruptions: Nature Geoscience, v. 13, p. 163–169, https://doi.org/10.1038/s41561-019-0520-6.
- Lee, C.-T.A., and Morton, D.M., 2015, High silica granites: Terminal porosity and crystal settling in shallow magma chambers: Earth and Planetary Science Letters, v. 409, p. 23–31, https:// doi.org/10.1016/j.epsl.2014.10.040.
- Lee, C.-T.A., Morton, D.M., Farner, M.J., and Moitra, P., 2015, Field and model constraints on silicic melt segregation by compaction/hindered settling: The role of water and its effect on latent heat release: American Mineralogist, v. 100, p. 1762–1777, https://doi.org/10.2138/am-2015-5121.
- Luhr, J.F., and Carmichael, I.S.E., 1980, The Colima Volcanic complex, Mexico: Contributions to Mineralogy and Petrology, v. 71, p. 343–372, https://doi.org/10.1007/BF00374707.
- Mantle, G.W., and Collins, W.J., 2008, Quantifying crustal thickness variations in evolving orogens: Correlation between arc basalt composition and Moho depth: Geology, v. 36, p. 87–90, https://doi.org/10.1130/G24095A.1.
- Marcotte, S.B., Klepeis, K.A., Clarke, G.L., Gehrels, G., and Hollis, J.A., 2005, Intra-arc transpression in the lower crust and its relationship to magmatism in a Mesozoic magmatic arc: Tectonophysics, v. 407, p. 135–163, https://doi.org/10.1016/j.tecto.2005.07.007.
- McCarthy, T.S., and Groves, D.I., 1979, The Blue Tier Batholith, northeastern Tasmania: Contributions to Mineralogy and Petrology, v. 71, p. 193–209, https://doi.org/10.1007/BF00375436.
- McCarthy, T.S., and Hasty, R.A., 1976, Trace element distribution patterns and their relationship to the crystallization of granitic melts: Geochimica et Cosmochimica Acta, v. 40, p. 1351–1358, https://doi.org/10.1016/0016-7037(76)90125-3.
- McCulloch, M.T., Bradshaw, J.Y., and Taylor, S.R., 1987, Sm-Nd and Rb-Sr isotopic and geochemical systematics in Phanerozoic granulites from Fiordland, southwest New Zealand: Contributions to Mineralogy and Petrology, v. 97, p. 183–195, https://doi.org/10.1007/BF00371238.
- McDonough, W.F., and Sun, S.-s., 1995, The composition of the Earth: Chemical Geology, v. 120, p. 223–253, https://doi.org/10.1016/0009-2541(94)00140-4.
- Milan, L.A. Daczko, N.R., Clarke, G.L., and Allibone, A.H., 2016, Complexity of in-situ zircon U-Pb-Hf isotope systematics during arc magma genesis at the roots of a Cretaceous arc, Fiordland, New Zealand: Lithos, v. 264, p. 296–314, https://doi.org/10.1016/j.lithos.2016.08.023.
- Milan, L.A., Daczko, N.R., and Clarke, G.L., 2017, Cordillera Zealandia: A Mesozoic arc flare-up on the palaeo-Pacific Gondwana Margin: Scientific Reports, v. 7, 261, https://doi.org/10.1038/s41598-017-00347-w.
- Miller, C.F., Furbish, D.J., Walker, B.A., Claiborne, L.L., Koteas, G.C., Bleick, H.A., and Miller, J.S., 2011, Growth of plutons by incremental emplacement of sheets in crystal-rich host: Evidence from Miocene intrusions of the Colorado River region, Nevada, USA: Tectonophysics, v. 500, p. 65–77, https://doi.org/10.1016/j.tecto.2009.07.011.
- Morimoto, N., 1988, Nomenclature of pyroxenes: Mineralogy and Petrology, v. 39, p. 55–76, https://doi.org/10.1007/BF01226262.
- Mortimer, N., Tulloch, A.J., Spark, R.N., Walker, N.W., Ladley, E., Allibone, A., and Kimbrough, D.L., 1999, Overview of the Median Batholith, New Zealand: A new interpretation of the geology

- of the Median Tectonic Zone and adjacent rocks: Journal of African Earth Sciences, v. 29, p. 257–268, https://doi.org/10.1016/S0899-5362(99)00095-0.
- Mortimer, N., Rattenbury, M.S., King, P.R., Bland, K.J., Barrell, D.J.A., Bache, F., Begg, J.G., Campbell, H.J., Cox, S.C., Crampton, J.S., Edbrooke, S.W., Forsyth, P.J., Johnston, M.R., Jongens, R., Lee, J.M., Leonard, G.S., Raine, J.I., Skinner, D.N.B., Timm, C., Townsend, D.B., Tulloch, A.J., Turnbull, I.M., and Turnbull, R.E., 2014, High-level stratigraphic scheme for New Zealand rocks: New Zealand Journal of Geology and Geophysics, v. 57, p. 402–419, https://doi.org/10.1080/00288306.2014.946062.
- Mortimer, N., Campbell, H.J., Tulloch, A.J., King, P.R., Stagpoole, V.M., Wood, R.A., Rattenbury, M.S., Sutherland, R., Adams, C.J., Collot, J., and Seton, M., 2017, Zealandia: Earth's Hidden Continent: GSA Today, v. 27, no. 3, p. 27–35, https://doi.org/10.1130/GSATG321A.1.
- Muir, R.J., Weaver, S.D., Bradshaw, J.D., Eby, G.N., and Evans, J.A., 1995, The Cretaceous Separation Point batholith, New Zealand. Granitoid magmas formed by melting of mafic lithosphere: Journal of the Geological Society, v. 152, p. 689–701, https://doi.org/10.1144 /usjgs.152.4.0689.
- Neave, D.A., and Putirka, K.D., 2017, A new clinopyroxene-liquid barometer, and implications for magma storage pressures under Icelandic rift zones: American Mineralogist, v. 102, p. 777–794, https://doi.org/10.2138/am-2017-5968.
- Oliver, G.J.H., 1977, Feldspathic hornblende and garnet granulites and associated anorthosite pegmatites from Doubtful Sound, Fiordland, New Zealand: Contributions to Mineralogy and Petrology, v. 65, p. 111–121, https://doi.org/10.1007/BF00371051.
- Oliver, G.J.H., 1980, Geology of the granulite and amphibolite facies gneisses of Doubtful Sound, Fiordland, New Zealand: New Zealand Journal of Geology and Geophysics, v. 23, p. 27–41, https://doi.org/10.1080/00288306.1980.10424190.
- Paton, C., Hellstrom, J., Paul, B., Woodhead, J., and Hergt, J., 2011, Iolite: Freeware for the visualisation and processing of mass spectrometric data: Journal of Analytical Atomic Spectrometry, v. 26. p. 2508–2518. https://doi.org/10.1039/c1ia10172b.
- Petford, N., and Atherton, M., 1996, Na-rich partial melts from newly underplated basaltic crust: The Cordillera Blanca Batholith, Peru: Journal of Petrology, v. 37, p. 1491–1521, https://doi.org/10.1093/petrology/37.6.1491.
- Profeta, L., Ducea, M.N., Chapman, J.B., Paterson, S.R., Gonzales, S.M.H., Kirsch, M., Petrescu, L., and DeCelles, P.G., 2015, Quantifying crustal thickness over time in magmatic arcs: Scientific Reports, v. 5, 17786, https://doi.org/10.1038/srep17786.
- Putirka, K.D., 2008, Thermometers and barometers for volcanic systems: Reviews in Mineralogy and Geochemistry, v. 69, p. 61–120, https://doi.org/10.2138/rmg.2008.69.3.
- Ramezani, J., and Tulloch, A.J., 2009, TIMS U-Pb geochronology of dioritic-granitic rocks Fiordland: GNS Science, Techfile Report, QMP Fiordlard/59, https://doi.org/10.21420/G2CC7Z.
- Ringwood, M.F., Schwartz, J.J., Turnbull, R.E., and Tulloch, A.J., 2021, Phanerozoic record of mantle-dominated arc magmatic surges in the Zealandia Cordillera: Geology, v. 49, p. 1230–1234, https://doi.org/10.1130/G48916.1.
- Rudnick, R.L., 1995, Making continental crust: Nature, v. 378, p. 571–578, https://doi.org/10.1038/378571a0.
- Rudnick, R.L., and Gao, S., 2013, Composition of the continental crust, *in* Holland, H.D., and Turekian, K.K., eds., Treatise on Geochemistry, 2<sup>nd</sup> edition: Elsevier, p. 1–51.
- Schaen, A.J., Singer, B.S., Cottle, J.M., Garibaldi, N., Schoene, B., Satkoski, A.M., and Fournelle, J., 2018, Textural and mineralogical record of low-pressure melt extraction and silicic cumulate formation in the Late Miocene Risco Bayo–Huemul Plutonic Complex, southern Andes: Journal of Petrology, v. 59, p. 1991–2016, https://doi.org/10.1093/petrology/egv087.
- Schwartz, J.J., Stowell, H.H., Klepeis, K.A., Tulloch, A.J., Kylander-Clark, A.R.C., Hacker, B.R., and Coble, M.A., 2016, Thermochronology of extensional orogenic collapse in the deep crust of Zealandia: Geosphere. v. 12. p. 647–677. https://doi.org/10.1130/GES01232.1.
- Schwartz, J.J., Klepeis, K.A., Sadorski, J.F., Stowell, H.H., Tulloch, A.J., and Coble, M.A., 2017, The tempo of continental arc construction in the Mesozoic Median Batholith, Fiordland, New Zealand: Lithosphere, v. 9, p. 343–365, https://doi.org/10.1130/L610.1.
- Schwartz, J.J., Andico, S., Turnbull, R.E., Klepeis, K.A., Tulloch, A.J., Kitajima, K., and Valley, J.W., 2021, Stable and transient isotopic trends in the crustal evolution of Zealandia Cordillera: American Mineralogist, v. 106, p. 1369–1387, https://doi.org/10.2138/am-2021-7626.
- Scott, J.M., Cooper, A.F., Palin, J.M., Tulloch, A.J., Kula, J., Jongens, R., Spell, T.L., and Pearson, N.J., 2009, Tracking the influence of a continental margin on growth of a magmatic arc, Fiordland, New Zealand, using thermobarometry, thermochronology, and zircon U-Pb and Hf isotopes: Tectonics, v. 28, TC6007, https://doi.org/10.1029/2009TC002489.

- Scott, J.M., Cooper, A.F., Tulloch, A.J., and Spell, T.L., 2011, Crustal thickening of the Early Cretaceous paleo-Pacific Gondwana margin: Gondwana Research, v. 20, p. 380–394, https://doi.org/10.1016/j.gr.2010.10.008.
- Severs, M.J., Beard, J.S., Fedele, L., Hanchar, J.M., Mutchler, S.R., and Bodnar, R.J., 2009, Partitioning behavior of trace elements between dacitic melt and plagioclase, orthopyroxene, and clinopyroxene based on laser ablation ICPMS analysis of silicate melt inclusions: Geochimica et Cosmochimica Acta, v. 73, p. 2123–2141, https://doi.org/10.1016/j.gca.2009.01.009.
- Sisson, T.W., 1991, Pyroxene-high silica rhyolite trace element partition coefficients measured by ion microprobe: Geochimica et Cosmochimica Acta, v. 55, p. 1575–1585, https://doi.org/10.1016/0016-7037(91)90129-S.
- Stevenson, J.A., Daczko, N.R., Clarke, G.L., Pearson, N., and Klepeis, K.A., 2005, Direct observation of adakite melts generated in the lower continental crust, Fiordland, New Zealand: Terra Nova, v. 17, p. 73–79, https://doi.org/10.1111/j.1365-3121.2004.00586.x.
- Stowell, H., Odom Parker, K., Gatewood, M., Tulloch, A., and Koenig, A., 2014, Temporal links between pluton emplacement, garnet granulite metamorphism, partial melting and extensional collapse in the lower crust of a Cretaceous magmatic arc, Fiordland, New Zealand: Journal of Metamorphic Geology, v. 32, p. 151–175, https://doi.org/10.1111/jmg.12064.
- Stowell, H.H., Schwartz, J.J., Klepeis, K.A., Hout, C., Tulloch, A.J., and Koenig, A., 2017, Sm-Nd garnet ages for granulite and eclogite in the Breaksea Orthogneiss and widespread granulite facies metamorphism of the lower crust, Fiordland magmatic arc, New Zealand: Lithosphere, v. 9, p. 953–975, https://doi.org/10.1130/L662.1.
- Taylor, S.R., and McLennan, S.M., 1985, The Continental Crust: Its Composition and Evolution: Boston, Massachusetts, Blackwell Scientific, 312 p.
- Taylor, S.R., and McLennan, S.M., 1995, The geochemical evolution of the continental crust: Reviews of Geophysics, v. 33, p. 241–265, https://doi.org/10.1029/95RG00262.
- Tulloch, A.J., and Kimbrough, D.L., 2003, Paired plutonic belts in convergent margins and the development of high Sr/Y magmatism: Peninsular Ranges Batholith of Baja California and Median Batholith of New Zealand, in Johnson, S.E., Paterson, S.R., Fletcher, J.M., Girty, G.H., Kimbrough, D.L., and Martín-Barajas, A., eds., The Tectonic Evolution of Northwestern Mexico and the Southwestern USA: Geological Society of America Special Paper 374, p. 275–295, https://doi.org/10.1130/0-8137-2374-4.275.
- Tulloch, A., and Palin, M., 2013, Provenance of detrital feldspar: Calibration of an LA-ICPMS trace element chemistry finger printing tool: GNS Science Report 2012/35, 18 p.
- Tulloch, A.J., Ramezani, J., Mortimer, N., Mortensen, J., van den Bogaard, P., and Maas, R., 2009, Cretaceous felsic volcanism in New Zealand and Lord Howe Rise (Zealandia) as a precursor to final Gondwana break-up, in Ring, U., and Wernicke, B., eds., Extending a Continent: Architecture, Rheology and Heat Budget: Geological Society of London Special Publication 321, p. 89–118, https://doi.org/10.1144/SP321.5.

- Turnbull, R.E., Weaver, S., Tulloch, A., Cole, J., Handler, M., and Ireland, T., 2010, Field and geochemical constraints on mafic-felsic interactions, and processes in high-level arc magma chambers: An example from the Halfmoon Pluton, New Zealand: Journal of Petrology, v. 51, p. 1477–1505, https://doi.org/10.1093/petrology/eqq026.
- Ulmer, P., Kaegi, R., and Müntener, O., 2018, Experimentally derived intermediate to silica-rich arc magmas by fractional and equilibrium crystallization at 1.0 GPa: An evaluation of phase relationships, compositions, liquid lines of descent and oxygen fugacity: Journal of Petrology, v. 59, no. 1, p. 11–58, https://doi.org/10.1093/petrology/egy017.
- Vernon, R.H., and Collins, W.J., 2011, Structural criteria for identifying granitic cumulates: The Journal of Geology, v. 119, p. 127–142, https://doi.org/10.1086/658198.
- Watson, E.B., and Harrison, T.M., 1983, Zircon saturation revisited: Temperature and composition effects in a variety of crustal magma types: Earth and Planetary Science Letters, v. 64, p. 295–304, https://doi.org/10.1016/0012-821X(83)90211-X.
- Werts, K., Barnes, C.G., Memeti, V., Ratschbacher, B., Williams, D., and Paterson, S.R., 2020, Hornblende as a tool for assessing mineral-melt equilibrium and recognition of crystal accumulation: American Mineralogist, v. 105, p. 77–91, https://doi.org/10.2138/am-2020 .6972
- Wiebe, R.A., 1993, The Pleasant Bay layered gabbro-diorite, coastal Maine: Ponding and crystallization of basaltic injections into a silicic magma chamber: Journal of Petrology, v. 34, p. 461–489, https://doi.org/10.1093/petrology/34.3.461.
- Wiebe, R.A., Blair, K.D., Hawkins, D.P., and Sabine, C.P., 2002, Mafic injections, in situ hybridization, and crystal accumulation in the Pyramid Peak granite, California: Geological Society of America Bulletin, v. 114, p. 909–920, https://doi.org/10.1130/0016-7606(2002)114<0909: MISHA>2.0.CO:2.
- Wood, B.J., and Trigila, R., 2001, Experimental determination of aluminous clinopyroxene-melt partition coefficients for potassic liquids, with application to the evolution of the Roman province potassic magmas: Chemical Geology, v. 172, p. 213–223, https://doi.org/10.1016/ /S0009-2541(00)00259-X.
- Yogodzinski, G.M., and Kelemen, P.B., 1998, Slab melting in the Aleutians: Implications of an ion probe study of clinopyroxene in primitive adakite and basalt: Earth and Planetary Science Letters, v. 158, p. 53–65, https://doi.org/10.1016/S0012-821X(98)00041-7.
- Zeng, Y., Ducea, M.N., Xu, J., Chen, J., and Dong, Y.-H., 2020, Negligible surface uplift following foundering of thickened central Tibetan lower crust: Geology, v. 49, p. 45–50, https://doi.org /10.1130/G48142.1.
- Zhang, J., Humphreys, M.C.S., Cooper, G.F., Davidson, J.P., and Macpherson, C.G., 2017, Magma mush chemistry at subduction zones, revealed by new melt major element inversion from calcic amphiboles: American Mineralogist, v. 102, p. 1353–1367, https://doi.org/10.2138/am -2017-5928.